AGU PUBLICATIONS

JGR

Journal of Geophysical Research: Solid Earth

RESEARCH ARTICLE
10.1002/2017JB014749

Key Points:
- A new fault slip model satisfactorily reproduces global seismic waves, basin-wide tsunami waveforms, and regional coastal runup
- Iterative seismic wave inversion and forward tsunami modeling achieve self-consistency and give reasonable prediction of geodetic data
- Observed tsunami waveforms and runup heights do not require an exotic source undetected in seismic or geodetic data

Supporting Information:
- Supporting Information S1
- Data Set S1
- Data Set S2
- Movie S1

Correspondence to:
K. F. Cheung,
cheung@hawaii.edu

Citation:
Yamazaki, Y., Cheung, K. F., & Lay, T. (2018). A self-consistent fault slip model for the 2011 Tohoku earthquake and tsunami. *Journal of Geophysical Research: Solid Earth*, *123*, 1435–1458. https://doi.org/10.1002/2017JB014749

Received 20 JUL 2017
Accepted 25 DEC 2017
Accepted article online 29 DEC 2017
Published online 7 FEB 2018

A Self-Consistent Fault Slip Model for the 2011 Tohoku Earthquake and Tsunami

Yoshiki Yamazaki[1], Kwok Fai Cheung[1], and Thorne Lay[2]

[1]Department of Ocean and Resources Engineering, University of Hawai'i at Mānoa, Honolulu, HI, USA, [2]Department of Earth and Planetary Sciences, University of California, Santa Cruz, CA, USA

Abstract The unprecedented geophysical and hydrographic data sets from the 2011 Tohoku earthquake and tsunami have facilitated numerous modeling and inversion analyses for a wide range of dislocation models. Significant uncertainties remain in the slip distribution as well as the possible contribution of tsunami excitation from submarine slumping or anelastic wedge deformation. We seek a self-consistent model for the primary teleseismic and tsunami observations through an iterative approach that begins with downsampling of a finite fault model inverted from global seismic records. Direct adjustment of the fault displacement guided by high-resolution forward modeling of near-field tsunami waveform and runup measurements improves the features that are not satisfactorily accounted for by the seismic wave inversion. The results show acute sensitivity of the runup to impulsive tsunami waves generated by near-trench slip. The adjusted finite fault model is able to reproduce the DART records across the Pacific Ocean in forward modeling of the far-field tsunami as well as the global seismic records through a finer-scale subfault moment- and rake-constrained inversion, thereby validating its ability to account for the tsunami and teleseismic observations without requiring an exotic source. The upsampled final model gives reasonably good fits to onshore and offshore geodetic observations albeit early after-slip effects and wedge faulting that cannot be reliably accounted for. The large predicted slip of over 20 m at shallow depth extending northward to ~39.7°N indicates extensive rerupture and reduced seismic hazard of the 1896 tsunami earthquake zone, as inferred to varying extents by several recent joint and tsunami-only inversions.

1. Introduction

The 2011 Tohoku earthquake from rupture of the megathrust off northeastern Honshu generated strong regional shaking and a devastating tsunami in the near field. The ground motions were captured in extensive recordings of regional and global seismic waves as well as geodetic land and seafloor displacements along the Tohoku coast. It was quickly established that large offshore slip of up to ~60 m produced the energetic tsunami waves reaching 5 to 6 m amplitude at offshore water-level stations surrounding the source (Fujii et al., 2011). Mori et al. (2011, 2012) compiled over 5,300 inundation and runup measurements from surveys of 300 scientists along 2,000 km of east Japan coasts. The compiled measurements provide an overall depiction of the tsunami impact, which includes 5 km of inundation on the coastal plain in Sendai and runup as high as 40 m along the Sanriku coast fronting the northern rupture region. The unprecedented geophysical and hydrographic data sets have been instrumental in reconstructing the earthquake rupture process and its relationship to the resulting tsunami waveforms and impacts along the Tohoku coast (Lay, 2017).

Analyses of various combinations of teleseismic and regional body and surface waves as well as GPS ground displacements across Japan have produced many models of the earthquake source (e.g., Ammon et al., 2011; Hayes, 2011; Ide et al., 2011; Iinuma et al., 2011, 2012; Ito et al., 2011; Koketsu et al., 2011; Koper et al., 2011; Kubo & Kakehi, 2013; Lay, Ammon et al., 2011; Lee, 2011; Minson et al., 2014; Miyazaki et al., 2011; Ozawa et al., 2011, 2012; Pollitz et al., 2011; Shao et al., 2011; Simons et al., 2011; Wei et al., 2012; Yagi & Fukahata, 2011; Yoshida et al., 2011; Yue & Lay, 2011, 2013). The models that emphasize geodetic static displacements on the Japanese mainland have a tendency to put the largest slip on the fault around or downdip from the hypocenter, while models based on teleseismic data tend to place very large slip offshore toward the trench. This discrepancy is primarily a result of poor spatial resolution from the one-sided distribution of the geodetic observations, but the seismic data also have limited resolution when analyzed alone. Inclusion of seafloor geodetic records (Kido et al., 2011; Sato et al., 2011) and repeat seismic reflection images that captured offset at the trench (Fujiwara et al., 2011) in the geodetic modeling increases the estimated near-trench slip (e.g., Iinuma et al., 2012; Ito et al., 2011; Yue & Lay, 2013).

Tsunami waves have much lower propagation speeds in comparison to rupture expansion and seismic waves, and their amplitudes and periods in the near field are sensitive to the coseismic seafloor movement. The records from well-positioned water-level stations around the source allow reliable inference of the seafloor deformation (e.g., Dettmer et al., 2016; Fujii et al., 2011; Hayashi et al., 2011; Hossen et al., 2015; Jiang & Simons, 2016; Maeda et al., 2011; Satake et al., 2013; Tang et al., 2012; Wei et al., 2013). The recorded tsunami waveforms, which provide constraints on the updip and along-strike extent of fault displacements, complement the geophysical data sets to provide a more complete account of the rupture through joint analysis or inversion (e.g., Bletery et al., 2014; Grilli et al., 2013; Gusman et al., 2012; Hooper et al., 2013; Lay, Yamazaki et al., 2011; Løvholt et al., 2012; Romano et al., 2012, 2014; Saito et al., 2011; Yamazaki, Lay, et al., 2011; Yamazaki et al., 2013; Yokota et al., 2011). Over 80 finite fault and finite source models have been published for the 2011 event; many salient aspects of the observations and models are discussed in reviews by Tajima et al. (2013), Hino (2015), Lorito et al. (2016), Sun et al. (2017), and Lay (2017). Most, but not all, of the tsunami-based models or joint analyses place the largest slip close to the trench. They vary substantially in detail due to a number of factors such as model parameterization, data set selection, and resolution of the different data types (Lay, 2017). Seismic and geodetic inversions of large earthquakes require highly parameterized and very detailed finite fault models, while inversions of tsunami observations are simpler in parameterization and have lower spatial and temporal resolutions due to the long-period waves.

Recognizing the complication caused by the varying resolution and sensitivity of the geophysical and tsunami data sets to distinct aspects of the rupture, Yamazaki, Lay, et al. (2011) took an intermediate approach with kinematic inversions of seismic and geodetic data being guided by forward modeling of tsunami signals around the source. Iterative adjustment of poorly constrained parameters, such as rupture velocity and total faulting extent, refines the rupture representation through progressively constrained seismic and geodetic inversions. This iterative approach, however, places more emphasis on the intrinsic resolution of the geophysical data sets, as the recorded tsunami waveforms do not directly determine details of the fault slip. The final finite fault model of such iteration produces good overall agreement with tsunami records from a number of recent events (Bai et al., 2014, 2017; Lay, Ye, Kanamori, Yamazaki, Cheung, Ammon, 2013; Lay, Ye, Kanamori, Yamazaki, Cheung, Kwong, et al., 2013; Li et al., 2016; Yue et al., 2014), but for the 2011 Tohoku tsunami, it does not fully describe the initial arrivals at coastal buoys adjacent to the southwestern and northern rupture regions (Yamazaki, Lay, et al., 2011). Direct inversion of the tsunami records alone can, of course, better fit the waveforms themselves (e.g., Fujii et al., 2011; Satake et al., 2013), but such models have not been explicitly reconciled with other data sets to demonstrate self consistency. Joint inversions of the tsunami waveforms with seismic and geodetic data can reconcile some of the discrepancies caused by limited resolution of different data types (e.g., Bletery et al., 2014; Melgar & Bock, 2015; Romano et al., 2014). However, there are still challenging issues of parameterization of the models and weighting of the diverse data sets.

There remain many questions about the various models for the 2011 Tohoku earthquake. For example MacInnes et al. (2013) compare tsunami predictions from 10 source models finding variable waveform discrepancies and consistent underprediction of coastal runup north of 39°. Tappin et al. (2014) assert that the models consistent with seismic and geodetic data are not able to match the tsunami signals at the near-field buoys or the runup along the Sanriku coast as well as the dispersive waves at DART (Deep-ocean Assessment and Reporting of Tsunami) station 21418 about 600 km offshore. Grilli et al. (2013), MacInnes et al. (2013), and Tappin et al. (2014) infer that an additional tsunami source in the northern rupture region such as a submarine landslide or slump near the trench is needed to explain the observations. The existing seismic and geodetic models vary significantly in how far north slip extends along the trench, but it is clear that the downdip region of the megathrust off Sanriku does not have significant coseismic slip, as it appears to have broad stable sliding and large after slip (e.g., Ozawa et al., 2012; Ye et al., 2011). This weakly coupled region actually causes the seismic and geodetic models to have very low resolution of slip updip, where the 1896 Meiji tsunami earthquake occurred (Kanamori, 1972; Tanioka & Satake, 1996b). While some models for the 2011 rupture do have 5 to 15 m of near-trench slip overlapping part of the 1896 rupture zone (e.g., Bletery et al., 2014; Lee et al., 2011; Romano et al., 2014; Tang et al., 2012; Wei et al., 2013; Yamazaki et al., 2013), many have little or no slip north of 39° (e.g., Iinuma et al., 2012; Minson et al., 2014; Ozawa et al., 2012; Yue & Lay, 2013). The tsunami waveform inversion of Satake et al. (2013) has close to 30 m near-trench slip in the 1896 zone, but in their model, this slip takes place several minutes after the 150 s main rupture inferred from seismic and geodetic data. The extent of the 2011 rupture and the seismic potential for the 1896 zone remain open issues to be addressed.

The recorded runup and inundation on east Japan coasts clearly provide a useful data set for evaluation and improving portions of source models not resolvable by seismic, geodetic, and offshore tsunami waveform recordings (Grilli et al., 2013; Hooper et al., 2013; MacInnes et al., 2013; Satake et al., 2013; Wei et al., 2013). These data can be essential for resolving whether the 1896 source region ruptured in 2011 or remains locked, and for establishing whether faulting models can actually match the coastal and offshore tsunami observations or if an exotic source such as a slump is required to match the records. Since tsunami runup and inundation are highly nonlinear, it is not feasible to directly invert the complex observations for a fault slip model. We extend the iterative approach of Yamazaki, Lay, et al. (2011) to include a stage of high-resolution forward modeling of the coastal tsunami processes. Exploring the sensitivity of the computed runup and inundation to fault displacement in the otherwise poorly constrained northern and southern portions of the rupture provides an additional level of detail to supplement the point observations of tsunami waveforms. The updated finite fault model is then used in a constrained inversion of global seismic waves to evaluate self-consistency as well as the competing inferences on the slip distribution among the diverse observations of the 2011 Tohoku earthquake and tsunami.

2. Methodology

The shock-capturing nonhydrostatic model, NEOWAVE (Yamazaki, Cheung, Kowalik, et al., 2012; Yamazaki, Cheung, et al., 2011; Yamazaki et al., 2009), is well suited for describing the 2011 Tohoku tsunami as well as its impact along the eastern coasts of Japan. The staggered finite difference model is based on the nonlinear shallow-water equations coupled with a pressure Poisson equation in terms of the depth-averaged vertical velocity to account for weakly dispersive tsunami waves. A shock-capturing scheme ensures conservation of momentum across flow discontinuities, such as bores or hydraulic jumps, which tend to develop during the runup and drawdown processes. The vertical velocity term can also resolve the time history of seafloor deformation in concert with a finite fault solution for modeling of tsunami generation as well as the nonhydrostatic flow over steep continental and near-shore slopes. These features are instrumental in modeling near-field tsunamis, which are strongly influenced by detailed source characteristics and local bathymetry (Li et al., 2016; Yamazaki et al., 2013; Ye, Kanamori, et al., 2016; Yue et al., 2014, 2015). For practical applications, NEOWAVE incorporates a two-way grid-nesting scheme for modeling of multiscale processes with increasing resolution in the spherical coordinate system.

The computation requires five grid levels to cover an expanse of the northwest Pacific and to resolve the rugged Sanriku coastlines simultaneously. Figure 1 shows a set of the telescoping grids to illustrate the model setup and provide location maps for places, geographic features, and water-level stations of significance to this study (see Figures S1–S3 in the supporting information for the remaining five-level telescoping grid systems). The level-1 grid, which extends from Okinawa to the Kuril Islands at 2 arc min (~3,000 m) resolution, describes regional transformation of the tsunami and allows sufficient wave attenuation at the ocean boundaries for implementation of a radiation condition. The level-2 grid resolves the continental margin of northeast Japan, where the rupture and near-field water-level stations were located, with greater detail at 24 arc sec (~600 m). A series of level-3 grids at 6 arc sec (~150 m) resolution provide transition to level-4 grids at 1.2 arc sec (~30 m) for computation of wave runup and inundation along all the Pacific coasts of Kanto, Tohoku, and Hokkaido. The recorded runup well exceeds 30 m at Noda, Taro, Aneyoshi, Ryori, and Onagawa, which are modeled locally with an additional level of grids at 0.2 arc sec (~5 m) resolution. These level-5 grids also include pre-event breakwaters to the extent resolvable by the source data, but the modeling effort cannot include the observed damage due to the unknown timing.

The bathymetry comprises the 30 arc sec (~750 m) GEBCO data from British Oceanographic Data Centre, the 20 arc sec (~500 m) bathymetric grid supplied by Japan Meteorological Agency as well as the M7005 Digital Bathymetry Chart and near-shore digital nautical charts purchased from Japan Hydrographic Association. The topography includes the 50 m digital elevation model for all of Japan and 5 m post-event lidar within the level-5 grids from the Geospatial Information Authority of Japan. The Generic Mapping Tools (GMT) facilitates blending of the diverse data sets and generation of the computational grids (Wessel & Smith, 1995). We utilize a Manning coefficient of 0.025 for the subgrid roughness of the seafloor and 0.035 as an average value for arable lands, wood lands, and low- to medium-density residential areas commonly found along the Tohoku and Hokkaido coasts (Kotani et al., 1998; Murashima et al., 2008). Modeling runup and inundation at high-density residential and commercial areas, which are often protected by breakwaters and seawalls, is very challenging.

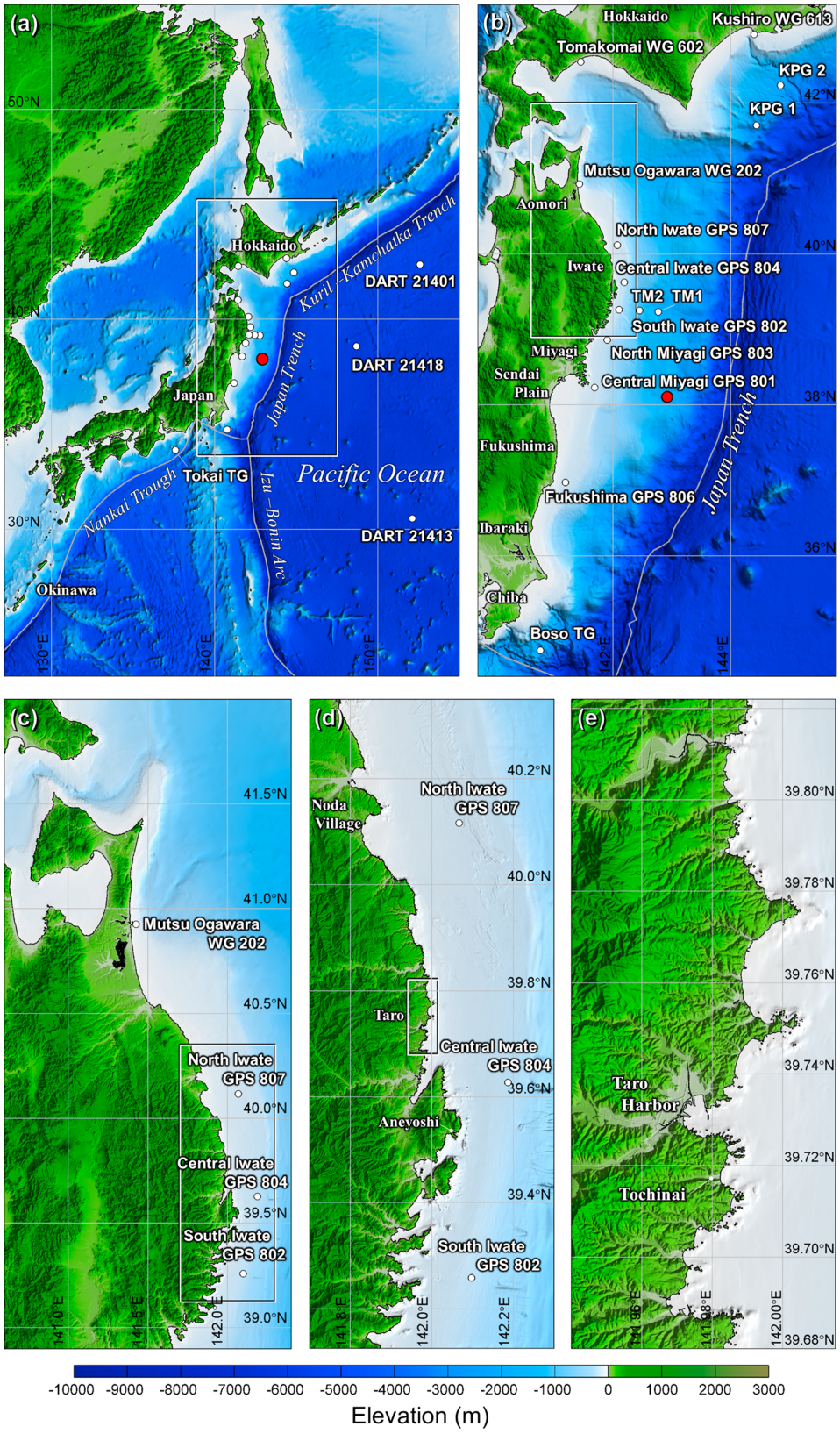

Figure 1. Location map, digital elevation model, and telescopic grid system for high-resolution runup and inundation modeling at Taro. (a) The level-1 grid with outline of the level-2 grid. (b) Close-up view of the level-2 grid along the Pacific coasts of Tohoku and Hokkaido. (c) The level-3 north Tohoku grid. (d) The level-4 Iwate grid. (e) The level-5 Taro grid. Red circle denotes the epicenter, white circles indicate water-level stations, and light grey lines trace along trenches.

The corresponding Manning coefficient varies from 0.04 to 0.08, but these are not considered due to sparse coverage of these high-density areas and uncertainties related to damage of coastal protection structures.

A reasonable starting model of the earthquake source is crucial for the iterative approach as the tsunami prediction from each iteration provides guidance to source refinement for the next. We examined a series of candidate models from joint seismic-geodetic inversion (Yue & Lay, 2013) and teleseismic inversion constrained by near-field tsunami modeling (Lay, Yamazaki, et al., 2011; Yamazaki, Lay, et al., 2011). The finite fault model P-MOD2 from seismic wave inversion by Lay, Yamazaki, et al. (2011) provides the best fit to the recorded tsunami waveforms among the models we considered, so it was selected as a starting point for the iterative refinement. Figure 2a plots the fault slip distribution and seafloor displacement over the 190 subfaults of 20×20 km^2 each based on a constant dip of 12° and uniform strike of 192° (increased in dip by 2° and rotated in strike by −10° from the original P-MOD2 based on tsunami modeling by Yamazaki, Lay, et al., 2011). The rupture begins 22.5 km (2.5 km deeper than the original) beneath the epicenter (38.107°N, 142.916°E) and propagates radially on the fault plane at 1.5 km/s for the first 100 km before increasing to 2.5 km/s farther out. The displacement duration on each subfault is up to 32 s, consisting of seven overlapping symmetric triangular 8 s duration subevents. The faulting lasts for 150 s overall with peak slip of 62 m near the trench. For tsunami modeling, the complex time functions are represented by a total subfault moment with an average rake and a total rise time. The crustal deformation deduced from the half-space solution of Okada (1992) includes subsidence along the Tohoku coast and distinct uplift patches at the epicenter and along the trench. The horizontal seafloor displacement reaches 46 m near the trench corroborating the seafloor geodetic records from Fujiwara et al. (2011), Ito et al. (2011), and Sato et al. (2011).

Model P-MOD2, with strike adjusted to 192°, is downsampled to a coarser grid with subfaults of 40×40 km^2 each and the rupture parameters and slip time histories are averaged to facilitate their iterative refinement. We extend the rupture area 40 km to the west and 20 km to the north into the regions not well resolved by the seismic inversion, yielding a starting model with 6×10 subfaults as shown in Figure 2b. A variable dip angle from 9° to 19° across the rupture area, based on the U.S. Geological Survey Slab 1.0 model (Hayes et al., 2012), improves consistency with the plate boundary geometry. The downsampling of the original slip distribution smoothes the seafloor displacement and widens the uplift patch along the trench but does not alter the overall seismic moment. The superposed vertical displacement time histories from the subfaults, augmented by the horizontal displacement on the slope (Tanioka & Satake, 1996a), define the land surface and seafloor movement for input to NEOWAVE (with exception of the topography for the five level-5 grids, which already includes the coseismic subsidence). The resulting tsunami matches the overall amplitude, waveform, and spectral content at 18 water-level stations surrounding the source but cannot resolve the impulsive initial peak off Iwate in the northern rupture region nor the broad initial wave at Central Miyagi and Fukushima in the south (Figure S4). Instead, the model produces a large impulsive peak immediately after the initial wave at the two southern locations. The computed runup fits the overall spatial pattern of the records albeit with notable overestimation at Central Miyagi and Fukushima and underestimation along the Sanriku coast in northern Iwate (Figure S5).

The near-field tsunami results from the starting model identify several areas for refinement. The mismatch of the weak initial arrival at the Fukushima GPS buoy suggests underestimation of the downdip slip in the southwest rupture region. The jerky main arrival at the buoy and the overestimated runup by 10 m on the Fukushima coast are due to the spurious extension of near-trench slip to the south, where the rupture is not spatially well resolved by seismic data (it can equally well be located to the north along the trench). At the Central Miyagi GPS, the computed jerky initial arrival and the large impulsive peak are artifacts of the modulated epicentral uplift patch and the concentrated near-trench slip immediately seaward. The large impulsive peak is responsible for overestimation of the runup by 15 m along the rugged Central Miyagi coasts. Conversely, the underestimation of runup for the most severely impacted Iwate coast and the poor resolution of the impulsive initial peak at the North and Central Iwate GPS buoys suggests omission of a large, localized near-trench tsunami excitation in the northeast rupture region that can generate short-period waves susceptible to amplification on the rugged shores. These disparities, akin to some of the deficiencies found by MacInnes et al. (2013) for other rupture models, provide guidance for initial adjustment of the slip and rake while retaining the other parameters in the finite fault model. Exploring the sensitivity of the computed waveforms and runup heights through extensive forward modeling leads us to an optimal fault slip distribution as shown in Figure 2c. The preferred tsunami-constrained model (T-MOD) shows shifting and spreading of the epicentral and downdip

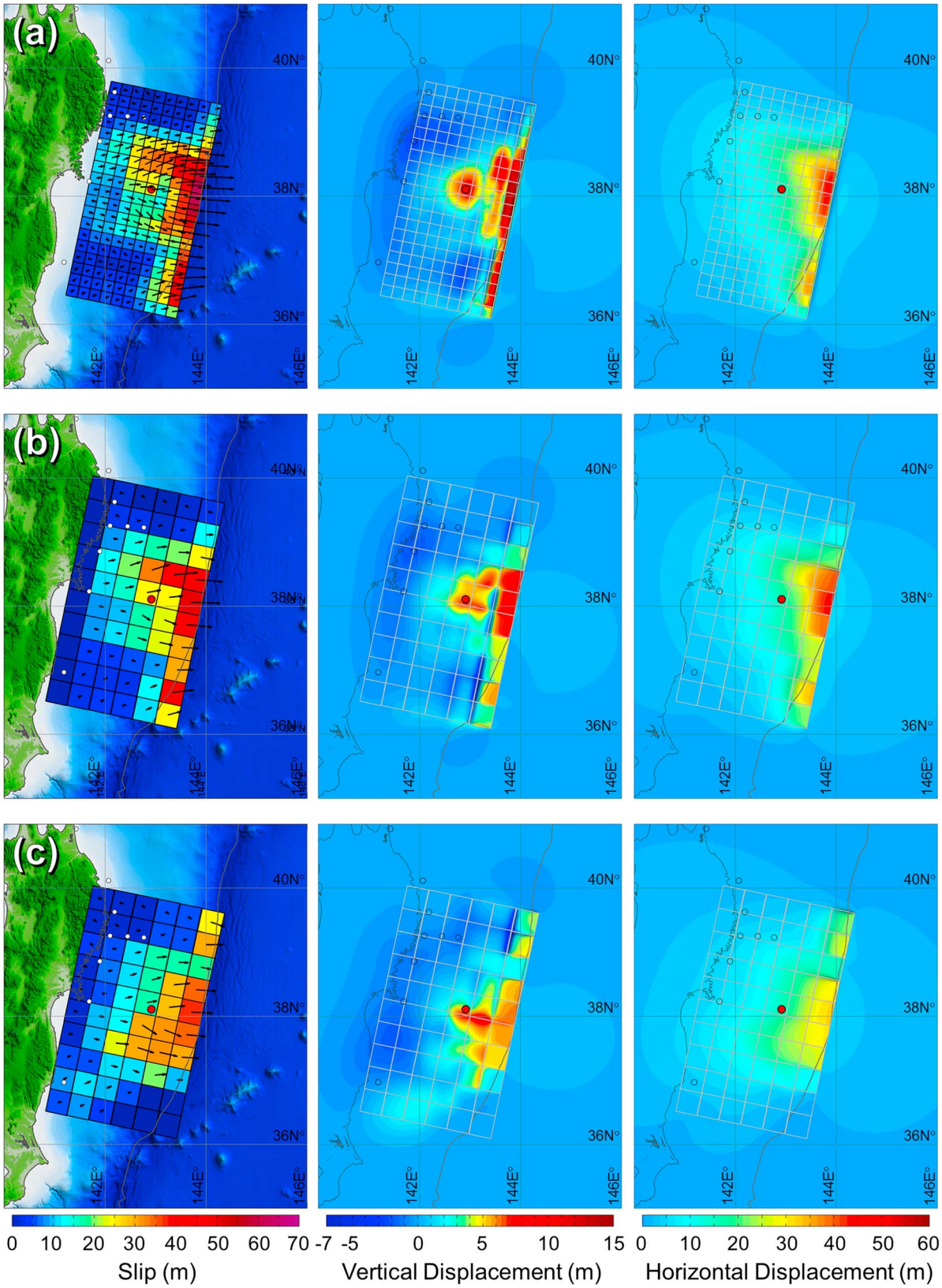

Figure 2. (left column) Model slip distribution, (middle column) vertical displacement, and (right column) horizontal displacement. (a) Initial model P-MOD2 from Lay, Yamazaki, et al. (2011) and Yamazaki, Lay, et al. (2011). (b) Downsampled starting model. (c) Preferred tsunami-constrained model, T-MOD. Red circle denotes the epicenter and white circles (left column) and open black circles (middle and right columns) indicate water-level stations.

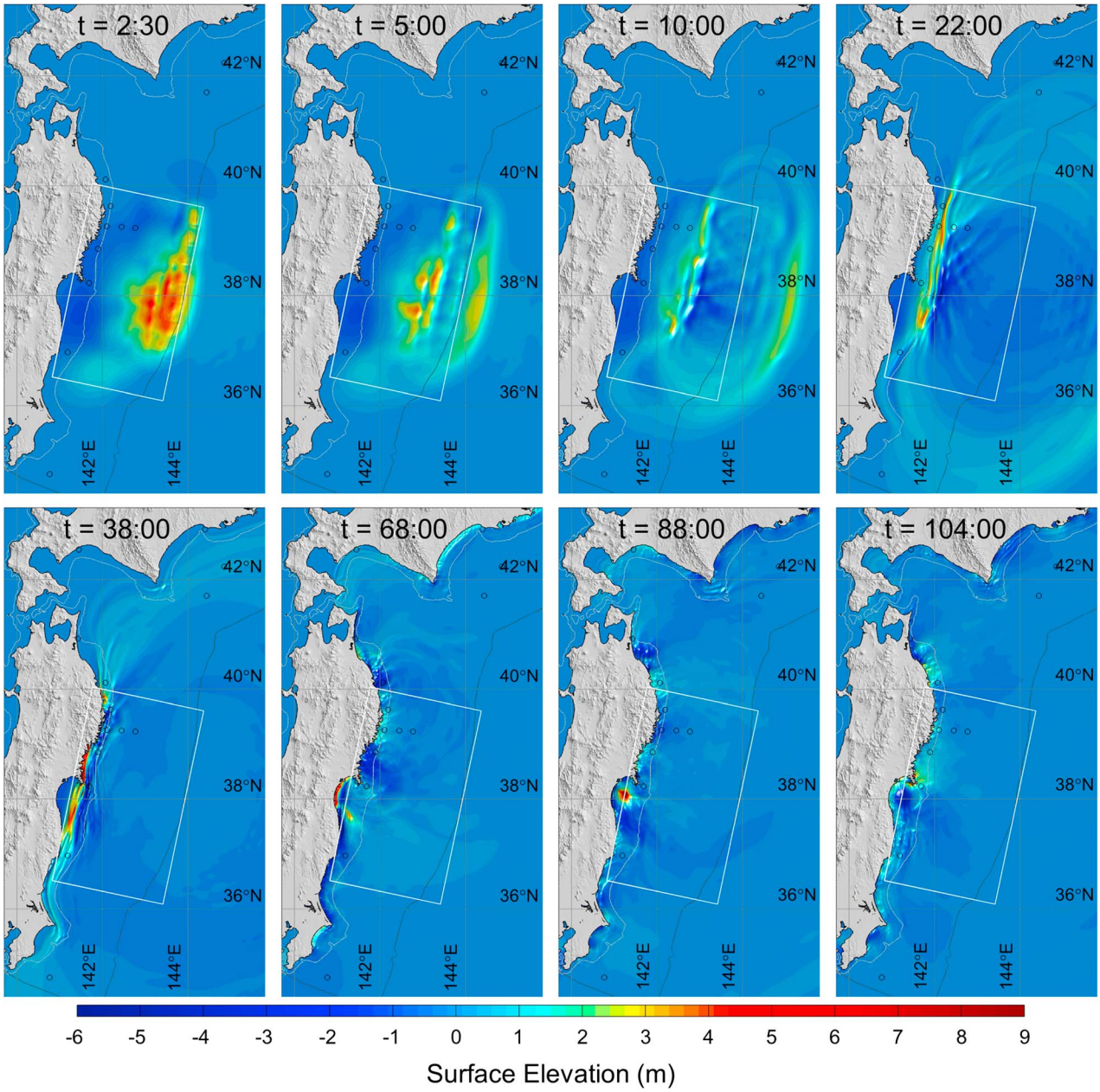

Figure 3. Surface elevation snapshots from Movie S1 for the preferred model T-MOD. Time is in minute and second after the earthquake origin time. Grey rectangle denotes the rupture area and dark grey line indicates the 200 m depth contour showing the approximate extent of the continental shelf.

slip to the south and the near-trench slip to the north. The uplift is now more evenly spread around the epicenter and along the trench, and the near-trench horizontal displacement is slightly reduced from the starting model (Data Set S1 in the supporting information provides the subfault parameters for T-MOD).

3. Tsunami Waveforms

The fault slip distribution and timing have strong influence on the tsunami generation process and the wave dynamics in the near field. Figure 3 shows a series of surface elevation snapshots from the preferred model T-MOD (see Movie S1 in the supporting information to aid interpretation of the results). The nonhydrostatic model NEOWAVE is instrumental in approximating the three-dimensional flow generated by the narrow uplift near the trench. Spreading of the seafloor-induced vertical flow in the horizontal directions results in a smoother initial pulse with smaller uplift at the sea surface. The generation of tsunami waves occurs

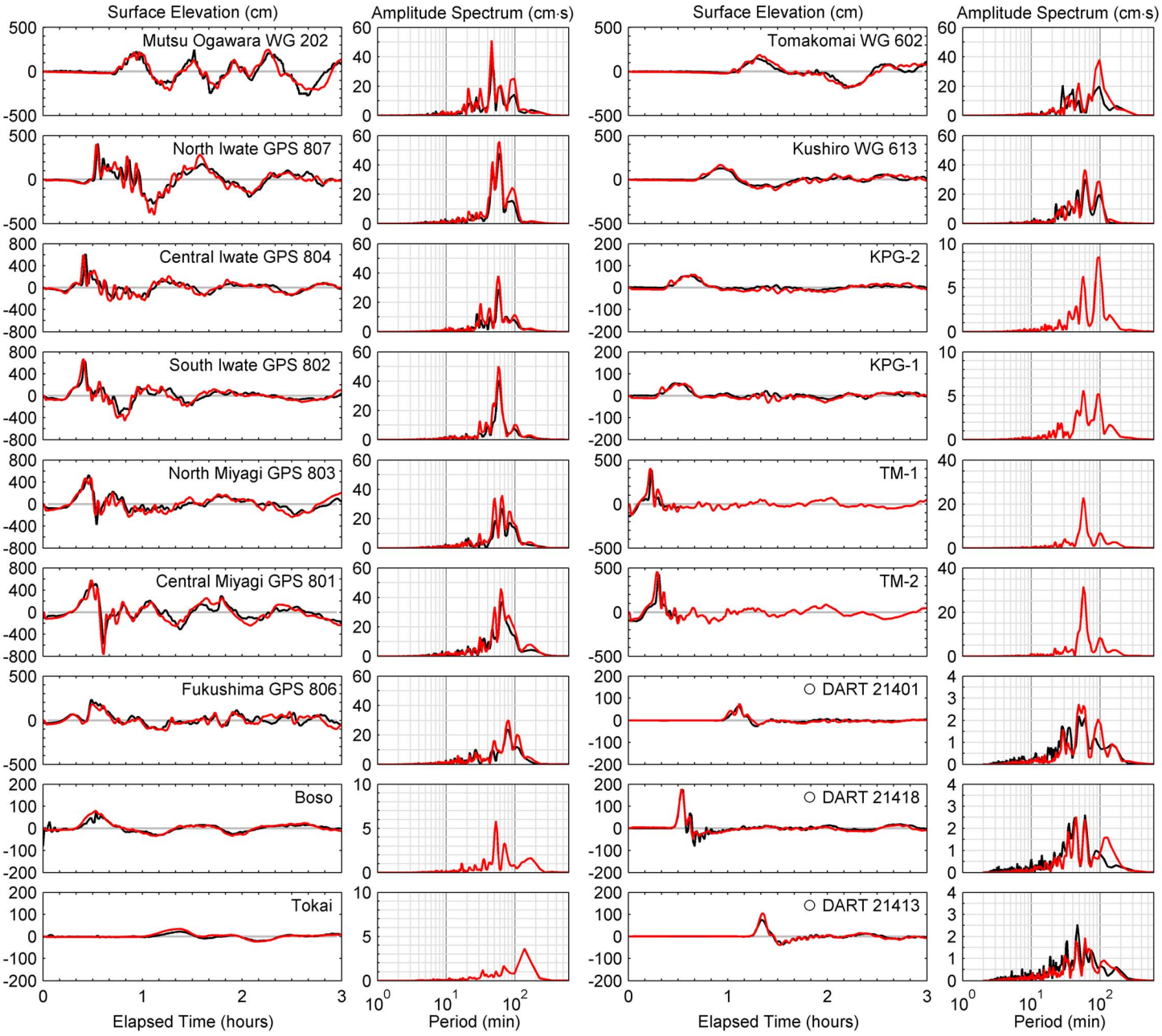

Figure 4. Comparison of recorded near-field tsunami waveforms and spectra (black lines) with results from the preferred model T-MOD (red lines). Spectra are not shown for records of less than 6 h duration.

simultaneously with their propagation away from the source. By the end of the rupture 2.5 min later, the tsunami has evolved considerably from the seafloor displacement shown in Figure 2c. The snapshots at 5 and 10 min show propagation of radial waves from the epicenter as well as a system of long-crested and diffracted waves originating from the near-trench uplift. The radial and long-crested waves simultaneously reach the Sanriku coast and enter Sendai Bay around 22 and 38 min after the faulting. The radial waves are ahead of the long-crested and diffracted waves between these two locations and vice versa to the north and south. Due to the wide shallow shelf at Sendai Bay, the initial wave does not reach the shore for another 30 min. The diffracted initial wave around Oshika Peninsula and the reflection from Fukushima reach Sendai Bay at 88 min and produce a second surge onto the Sendai plain at 104 min. The 200 m contour indicates the approximate extent of the continental shelf, which exhibits persistent edge wave activity long after the initial arrival.

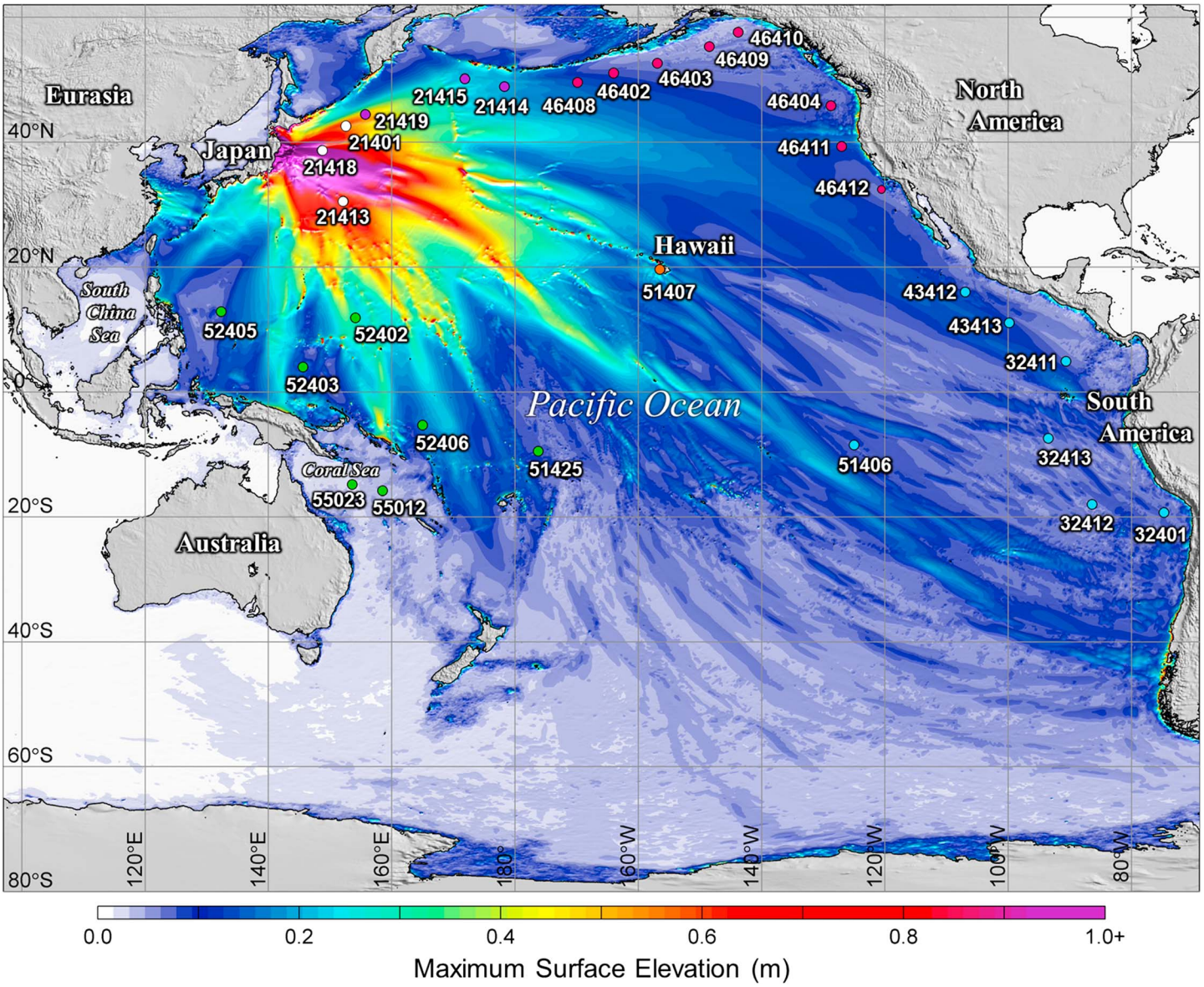

Figure 5. Maximum surface elevation of the 2011 Tohoku tsunami across the Pacific Ocean from the preferred model T-MOD. White/magenta, pink, blue, and green circles indicate DART buoys in northwest, northeast, southeast, and southwest sectors for referencing in text and Figure 6.

The well positioned GPS and DART buoys and coastal wave gauges provide nearly 360° azimuthal coverage of the near-field tsunami (see Figure 1 for location maps). Movie S1 is instrumental for interpretation of the recorded signals and the model results displayed in Figure 4. KPG-1 and KPG-2, located north of the rupture at ~2,200 m depth off the Hokkaido coast, recorded the diffracted waves from the near-trench rupture followed by attenuating radial waves from the epicentral uplift. The Kushiro, Tomakomai, and Mutsu Ogawara wave gauges at ~50 m depth detected the diffracted and radial waves from the source as well as subsequent edge waves over the continental shelf. The GPS buoys at 120 to 200 m water depth along the Iwate and Miyagi coasts provide a transect of the tsunami directly from the rupture. The model captures the impulsive wave from the trench immediately followed by the broad wave from the epicenter at the North Iwate buoy as well as superposition of the two wave systems with 5 to 6 m of combined amplitude at the Central and South Iwate buoys, corroborating the TM1 and TM2 measurements immediately offshore. The data sets at North and Central Miyagi show effects of the subsidence and lagging of the long-crested wave behind the radial wave resulting in more gentle arrivals followed by abrupt drop-off. The weak initial wave at Fukushima originates from the deep slip in the southwest rupture area, and the main arrival is

attributed to the epicentral and adjacent near-trench uplift, which also gives rise to the initial arrivals at Boso and Tokai to the south. With rapid attenuation of the radial waves, the deep-ocean DART records exhibit distinct signals of the long-crested wave from the trench.

The waveforms over 12 h after arrival are used to compute amplitude spectra of the tsunami. The frequency content shows notable but systematic variation from north to south associated with regional dominance of the primary wave components. KPG-1 and KPG-2 offshore of Hokkaido recorded strong signals of the radial waves at 60 min period from the epicenter and the diffracted waves at 90 min period associated with the length of the near-trench rupture. The nearby coastal buoys at Kushiro and Tomakomai register additional wave components around 45 min period related to the width of the near-trench rupture. The Mutsu Ogawara and North Iwate buoys to the south recorded stronger signals of 45 and 60 min period, while the 90 min diffracted waves diminish at buoys in front of the rupture region. The Iwate, Miyagi, and the TM stations recorded the strongest signal at 60 min period immediately landward of the epicenter. South of the rupture region, the 90 min signal from the trench becomes dominant at the Fukushima GPS buoy. Away from the source, the spectral signals at Boso and Tokai primarily reflect the local edge wave activities. The spectra at the three adjacent DART buoys show a 45 min dominant peak from the long-crested waves as well as a 30 min peak from leakage of standing edge waves over the shelf (Yamazaki et al., 2013). Dispersion causes attenuation of the leading wave amplitude and development of short-period trailing waves during propagation but does not alter the spectral content appreciably (Bai & Cheung, 2016).

There were another 26 DART buoys in operation across the Pacific during the 2011 Tohoku tsunami. The recorded waveforms, which are not used in the iterative refinement of the source model, provide an independent data set for validation. Figure 5 shows the locations of all 29 DART buoys along with the maximum surface elevation computed at 2 arc min resolution for 36 h elapsed time. The DART buoys provide very good coverage of the tsunami across the Pacific Ocean and well into the Coral Sea with detectable waves. There is also significant wave activity in East China Sea corroborated by tide gauge records of up to 0.5 m amplitude (Ren et al., 2013). The comparison of the computed and recorded data is arranged in four geographical sectors in Figure 6. The computed time series are shifted by up to 13 min to correct travel time errors associated with earth elasticity and water density variation (Baba et al., 2017; Tsai et al., 2013). The azimuthal distribution of the tsunami is strongly influenced by the primary wave components at 45, 60, and 90 min period and scattering by continental and insular shelves (Bai et al., 2015; Cheung et al., 2013; Yamazaki, Cheung, Pawlak, et al., 2012). The near-field and northwest Pacific stations recorded strong signals of the long-crested wave with 45 min period from the near-trench rupture followed by attenuating 60 min oscillations from the epicenter. Scattering and trapping along the Aleutian Islands and the Alaska continental margin weaken the initial long-crested wave and increases short-period oscillations as the tsunami propagates into the northeast sector. The long travel distance through many islands and seamount chains to the southeast completely obliterates the long-crested wave and introduces broadband oscillations off the Chile coast with subharmonics and superharmonics (Bai & Cheung, 2013). To the southwest of the tsunami source, the stations recorded strong 60 min signals from the epicenter as well as the diffracted waves from the trench at 90 min period.

The model results show clear improvements in comparison to predictions of the near-field signals from the starting model in Figure S4 and the far-field data from Bai et al. (2015) based on PMOD-2. As seen at the Iwate GPS buoys, the extension of the near-trench slip northward greatly improves the impulsive peak superposed on the much longer initial wave generated by the epicentral uplift. This has significant implications for coastal runup due to increased shoaling of the shorter-period wave over the continental margin. The shifting of the epicentral slip patch to the south and smoothing of the adjacent near-trench slip can better reproduce the initial arrivals at the two Miyagi GPS buoys. The truncation of the southern near-trench slip and extension of the downdip slip to the southwest portion of the fault model, which are necessary to reproduce the initial and main arrivals at Fukushima, also provide more accurate waveforms in the southwest Pacific into Coral Sea. The improved waveform predictions extend across the ocean, albeit with scattering and focusing by seamount and island chains, to the DART buoys in the northeast and southeast Pacific. Accurate waveform description over an extended duration at these distant locations requires precise reproduction of the amplitude, period, and phase of the wave components by the slip placement, tsunami generation, and dispersion process. The nonhydrostatic model, in the absence of earth elasticity and water density variation, predicts early arrivals by several minutes and neglects the small leading depression at buoys off the Chile coast. Other than that, the agreement between the model results

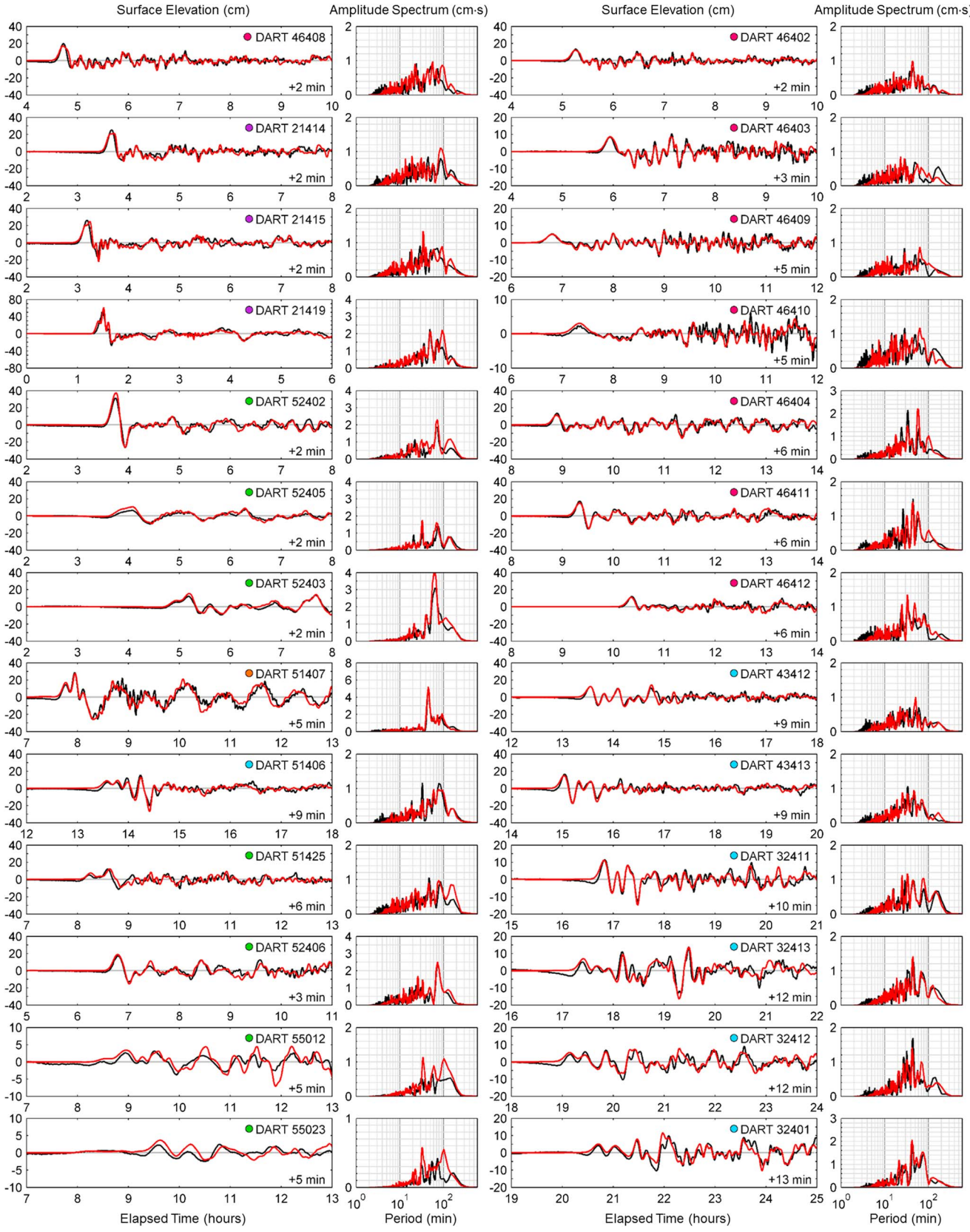

Figure 6. Comparison of recorded tsunami waveforms and spectra (black lines) with results from the preferred model T-MOD (red lines) around the Pacific Ocean by color-coded sectors as described in the caption of Figure 5. The modeled waveform is shifted by the indicated amount to match the recorded arrival time.

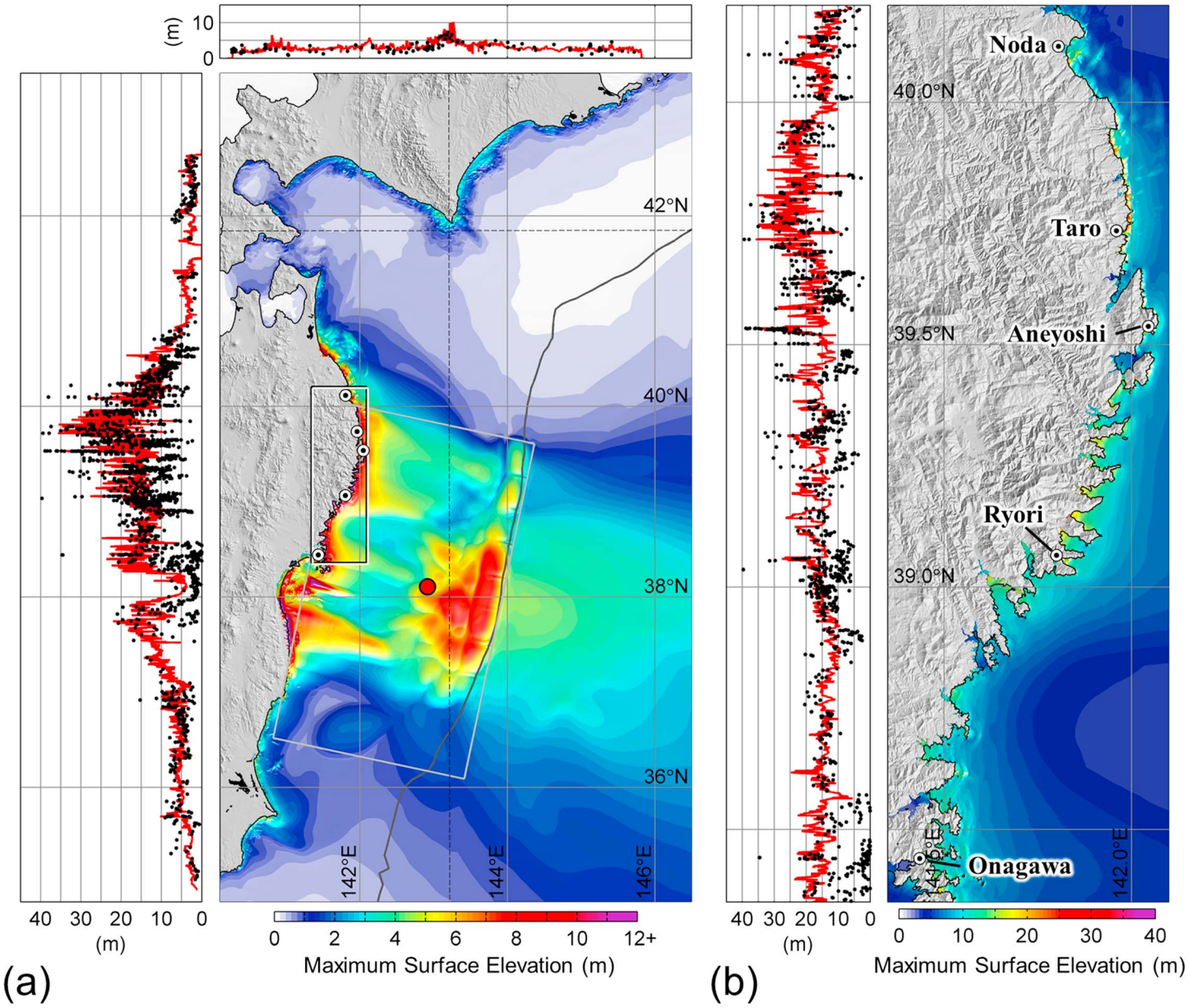

Figure 7. Comparison of recorded runup with results from the preferred model T-MOD. (a) East Japan coasts with the red circle denoting the epicenter and the light and dark grey lines indicating the rupture zone and the trench. Black dash lines divide the recorded and computed data into west and north sectors for projection of the runup shown at the left and top panels. (b) Sanriku coasts with high-resolution modeling at five severely impacted sites. Black dots and red lines denote recorded and computed runup.

and observations is remarkable given the vast extent of the coverage and the complex and varying wave patterns across the Pacific.

4. Tsunami Runup and Inundation

The runup and inundation measurements compiled by Mori et al. (2011) cover 2,000 km of Japan Pacific coasts from Chiba to Hokkaido and provide an important data set to confirm the overall fault slip distribution as well as the presence or absence of near-trench slip in the northern and southern rupture regions. We implemented a series of fault slip models, which fit the near-field waveform records well, for inundation computation with systems of telescopic grids to resolve the landform and inundation at 1.2 arc sec (~30 m) along these coastlines. This resolution is generally sufficient, except for several locations mostly along the rugged Iwate and North Miyagi coasts, which experienced the most severe impacts. In particular, the records show

extreme runup heights at isolated sites in Noda Village, Taro, Aneyoshi, Ryori, and Onagawa (see Figure 7 for location map). We model the runup at these sites, which are located at headlands or deep into ravines, with an additional level of nested grids to resolve the topography at 0.2 arc sec (~5 m). Field visits to the Tohoku coast in June 2011 and Aneyoshi, Taro, and Onagawa, in March 2013 provided additional site information to aid interpretation of the extreme runup records and their comparison with the model results.

Figure 7 compares the maximum surface elevation and runup from the preferred fault slip model T-MOD, which produces the optimal agreement with the measurements from Mori et al. (2011). The offshore sea surface elevation illustrates the distinct contributions from the epicentral uplift and near-trench slip to the tsunami. The resulting waves reach 6.9 and 10.6 m amplitude near the epicenter and along the trench in the main rupture region off Miyagi. The near-trench slip further north produces a narrow strip of sea surface uplift as high as 5.9 m. As inferred from the near-shore buoy records in Figure 4, the superposed leading radial and long-crested waves from the epicenter and trench result in large near-shore wave amplitude off the Sanriku coast despite being northward of the main rupture. The computed runup at the five sites with 0.2 arc sec (~5 m) resolution is concatenated with the output from the 1.2 arc sec (~30 m) grids. Projection of the maximum runup by latitude and longitude along the rugged coastlines results in a discontinuous distribution. The display shows multiple runup heights at approximately the same latitude or longitude, and only the envelopes of the model results and recorded data are directly comparable. The model results reproduce the general patterns of the recorded runup envelopes on the Tohoku and Hokkaido coasts facing the two principal dimensions of the rupture area. The computed runup follows closely the records of up to 20 m along the Fukushima coast with the truncation of near-trench slip in the southern rupture region. The southward shift of the epicentral slip and reduction of the adjacent near-trench slip result in much improved agreement of the runup along the Central Miyagi coast. On the other hand, the northern extension of near-trench slip is necessary to account for the persistent runup of over 30 m along the Sanriku coast.

Despite the good overall agreement, the model tends to overestimate the runup at low-lying high-density residential areas and often underestimates the extreme runup heights at headlands. Figure 8 shows detailed comparisons of the computed and recorded data over the 0.2 arc sec (~5 m) grids for an in-depth investigation. The records are flood elevations above the mean sea level, and their values along the inundation limit are runup heights. Noda Village is located immediately north of the rupture area on an open embayment. The large impulsive leading wave from the northern near-trench slip, as recorded by the North Iwate GPS buoy 20 km offshore, produced runup reaching 38.1 m as shown in Figure 8a. The model produces good general agreement with the measurements along most of the coastlines, but underestimates the peak runup at the northern headland of Maita. This localized discrepancy might be attributed to splashing of the impulsive wave on the steep slope that cannot be reproduced by the depth-integrated model. Overestimation of the computed inundation is found at the low-lying high-density residential area in the northern half of Noda Village. We utilize an average Manning coefficient typical of Tohuku terrain that is evidently low for the high-density residential areas.

Taro is located on an open coast 21 km northwest of the Central Iwate GPS, which recorded superposition of the impulsive long-crested wave and the broad radial wave from the main rupture region. The combined wave action produced the most severe impacts in the region. Figure 8b shows varying runup over the undulating terrains with gullies and headlands characteristic of the northern Iwate coast. The modeled tsunami floods the entire waterfront area of Taro Harbor to 22.2 m elevation, which corroborates recorded values of up to 20.7 m. The computed runup at the headland facing the harbor has a range of 9.0–22.2 m versus recorded values of 12.2–21.6 m. The second largest recorded runup of 39.4 m was at Tochinai, a ravine immediately south of Taro Harbor. The model gives 35.1 m slightly seaward of the location where the runup was recorded indicating the acute steepness in the upper reach of the ravine. Aneyoshi, located 20 km south of Taro, recorded the third largest runup of 38.9 m at a steep, winding ravine that opens to an alluvial plain fronting a cove. The modeled flow inundates the alluvial plain matching the records on the mountain slopes as shown in Figure 8c and stops at a 180° bend in the upper reach of the ravine at 33.6 m elevation. The model reproduces the flows over the challenging terrains at both locations reasonably well, but cannot fully capture the runup in narrow ravines less than 10 m wide even with 5 m grid resolution.

Ryori and Onagawa are located shoreward of the North and Central Miyagi GPS buoys, which recorded a gentle rise to a sharp peak and an abrupt drop-off associated with the lagging of the impulsive long-crested wave behind the broad radial wave. Ryori is at the head of a long, V-shape bay susceptible to wave amplification.

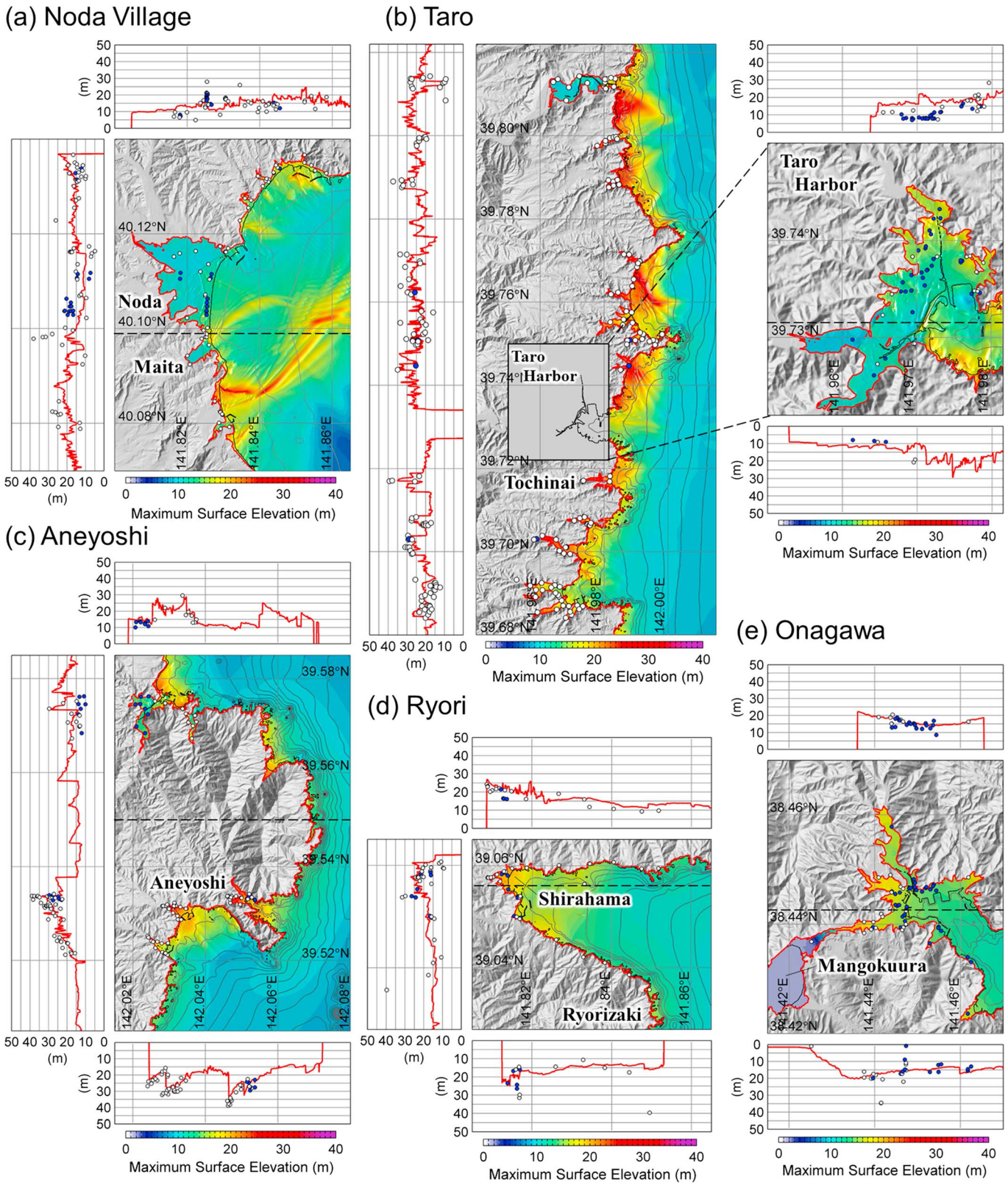

Figure 8. Comparison of recorded runup and inundation with results from the preferred model T-MOD at five severely impacted sites. (a) Noda Village. (b) Taro. (c) Aneyoshi. (d) Ryori. (e) Onagawa. Red lines indicate computed runup and inundation limit, white circles denote recorded runup, and blue circles denote the recorded flow depth plus land elevation. Black dashed line divides the recorded and computed data into north and south sectors for projection of the runup shown at the top and bottom panels of each figure. Grey lines indicate depth contours at 10 m intervals.

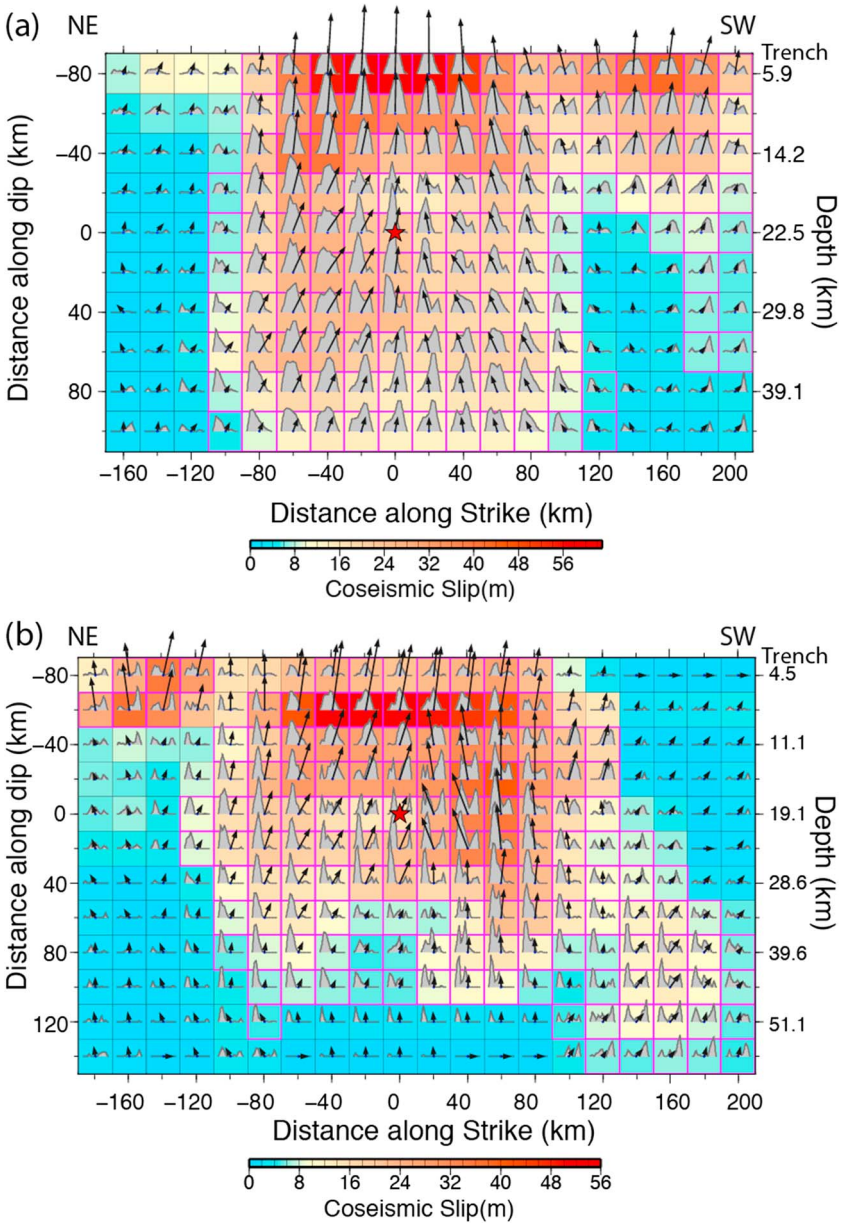

Figure 9. Slip distributions for the 2011 Tohoku earthquake. (a) Initial model P-MOD2 from Lay, Yamazaki et al. (2011) and Yamazaki, Lay, et al. (2011). (b) Final model TP-MOD upsampled from T-MOD through seismic inversion. The trench is along the upper boundary with the northern end of the fault on the left. The slip in each 20 × 20 km^2 subfault is indicated by the color palette and the vector oriented in the rake direction on the fault plane. The red stars indicate the hypocentral position. The subfault source time functions are indicated by the gray polygons within each subfault. The subfault source durations are 32 and 48 s long for P-MOD2 and TP-MOD. The corresponding moment rate functions are shown in Figure S7. Waveform fits for Figure 9b are shown in Figure S6. Depths include a 3.0 km deep-water layer.

Figure 8d shows good overall agreement of the recorded and computed runup heights on the two opposing shores. The model, however, cannot match the 31.5 m recorded runup on a headland south of Shirahama deep inside the bay due to a massive splash captured by video footage from TV Asahi ANN News (https://www.youtube.com/watch?v=n_lwAii93Qc) and the largest 39.7 m runup from the tsunami at Ryorizaki, a headland south of Ryori Bay, likely from another splash of the incoming flow. Onagawa saddles between an embayment and an inland sea. The tsunami entering from Onagawa Bay flooded most of the town (Suppasri et al., 2012) and overtopped a narrow passage over a ridge into the inland sea, Mangokuura. Figure 8e shows the modeled tsunami reaches 16 m elevation at the head of the bay and 18 m over the

ridge that agree well with the recorded values of 17.1–20.4 m and 16.0–20.1 m, respectively. The maximum recorded runup of 34.7 m, which is 14 m higher than the value recorded 40 m away, likely originated from splash-up of the flow on the mountain slope. The computed flow depth is only 0.2 m at the top of the ridge corroborating the observed water damage to building floor fixtures during our first field visit. The flood reaches over 1 km from the shore and 18 m elevation in an adjacent valley with a constricted entrance, where extensive scour was observed. Overall, the model provides a good match of the recorded runup and inundation at both locations in Miyagi.

5. Teleseismic Waves and Geodetic Static Motions

Given the good agreement with the tsunami waveforms and coastal impacts, the final stage of our iterative approach is to examine the consistency of the preferred model T-MOD with the teleseismic waveforms used in the initial model. We also consider how well the model predicts geodetic static motions in light of the discrepancies among the prior studies discussed in section 1. Despite the significant effects on the modeled coastal runup, the departures from the starting model based on P-MOD2 are not that dramatic (Figure 2). In order to have a basis for comparing the seismic fitting with earlier results, we resampled the 60-subfault coarse model by dividing each subfault into four 20×20 km^2 units while retaining the dip-varying fault geometry. The model is then inverted for a kinematic solution using the same set of teleseismic *P* waves as used in deriving P-MOD2 with similar kinematic parameters. A slightly increased subfault duration of 48 s allows for timing flexibility in the upsampled slip distribution. To retain features derived from the tsunami observations, we applied constraint equations on each set of four subfaults to weight the solution toward having the same seismic moment and average rake from the corresponding subfault in the coarse model. The resulting inversion fits the data to within 0.1% of that attained in P-MOD2 in terms of waveform power. Both models account for 94% of the waveform variability (see Figure S6 for the waveform comparison). Figure S7 compares the moment rate function from P-MOD2 with the final tsunami/*P*-wave model (TP-MOD), which has a total seismic moment of 4.0×10^{22} Nm (M_w 9.0), compatible with long-period determinations for the range $>$200 s (Data Set S2 in the supporting information provides the subfault parameters for TP-MOD).

The comparison in Figure 9 clarifies the evolution through the iterative procedure from our starting model perturbed from P-MOD2 to TP-MOD, with shifting of large slip at shallow depth to the northeastern rupture region and increased slip downdip in the southwestern end of the large epicentral slip patch. The peak slip in the northeast is as large as 36 m but is not robustly resolved in the individual subfaults in damped linear least squares solutions. Average slip in excess of 20 m is obtained in the north, and this is quite consistent with the tsunami-waveform inversion of Satake et al. (2013), indicating that the rigidity model used in the seismic inversions is not responsible for excessive slip. This demonstrates that the large slip located updip of the very low slip region along the Sanriku coast is compatible with the teleseismic data, although it is not resolved by the teleseismic data alone, as the lower slip in P-MOD2 is also acceptable. The other major difference in the models is the increase in slip southwestward from the hypocenter, which results from the improved modeling of the Central Miyagi and Fukushima GPS buoy data. The peak slip in the shallow slip patch updip from the hypocenter is 56 m, consistent with many other estimates of large-slip near the trench discussed earlier. The static stress drop for the final rupture model is 5.9 MPa using the slip-weighted procedure of Noda et al. (2013) (Figure S8). The circular stress drop procedure of Ye, Lay, et al. (2016) gives a static estimate of 6.1 MPa for this model. These average values and the variability in stress drop (with local values up to 37 MPa) across the slip region are compatible with those for many models, summarized by Brown et al. (2015). To ensure that the final seismic inversion did not degrade the tsunami modeling, we use the resulting upsampled model TP-MOD to compute the near-field waveforms (Figure S9). There are inconsequential differences from the results of the coarse model in Figure 4. This highlights the varying resolution and sensitivity of the seismic and tsunami records to the rupture process and supports the use of the coarse model in the iteratively refinement of the computed tsunami.

We have achieved a self-consistent model for the teleseismic and diverse tsunami observations. A half-space Okada (1992) calculation predicts onshore GPS static displacements and offshore GPS/Acoustic displacements for this model, TP-MOD. The results in Figure 10a have root-mean-square errors (RMSEs) of 0.19 and 0.47 m with respect to the 319 vertical and horizontal displacement observations in northern Honshu within the level-2 grid (Figure 1a), but not surprisingly, there are some discrepancies. The comparison of the on-land GPS observations is quite reasonable for horizontal displacements, and vertical displacements are fit less well,

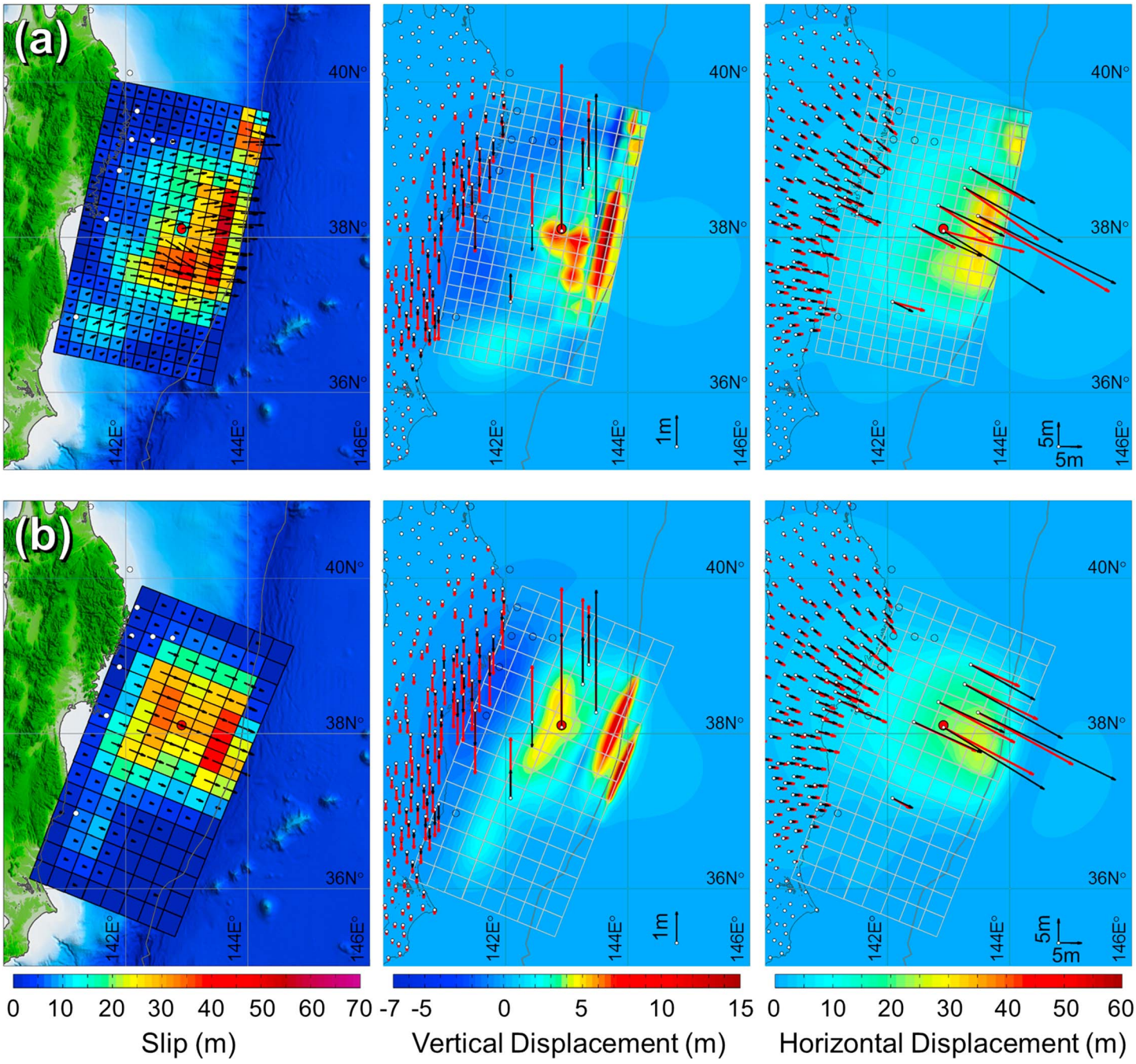

Figure 10. (left column) Model slip distribution, (middle column) computed and observed vertical displacements, and (right column) computed and observed horizontal displacements. (a) Final model TP-MOD. (b) Joint seismic-geodetic inversion from Yue and Lay (2013). Black arrows indicate subfault slip vectors in the left column. In the middle and right columns, black and red arrows indicate recorded and computed displacements at the locations indicated by small white circles. White cicrles in the left column and open black circles in the middle and right columns indicate locations of water level-stations.

but comparable to many models. Our model tends to slightly overpredict both horizontal and vertical displacements in the south, possibly because the seismic data provide limited resolution of slip in this part of the model and the tsunami fitting has not sufficiently spread the concentrated slip patch. The prediction of offshore GPS/Acoustic observations is not ideal, having RMSEs of 2.14 and 4.06 m with respect to the six vertical and seven horizontal displacement observations. There are substantial questions about how much early after-slip occurred prior to remeasurement of the GPS/Acoustic observations, with some studies assuming none and others assuming a large fraction of the total offset (see discussion in the

review by Lay, 2017). The offshore vertical motions have been difficult to match precisely in many studies as well and have attendant questions regarding influence by early normal faulting aftershocks in the wedge. The mismatch could also be partly due to the homogeneous, half-space assumption in the solution of Okada (1992) and our assumed constant slab geometry along the strike direction. Anisotropy and heterogeneity of crustal layers could have significant effects on the displacement (Masterlark, 2003).

For comparison, Figure 10b shows the slip distribution and vertical and horizontal displacements for the joint inversion of high-rate GPS, GPS/Acoustic, and seismic data by Yue and Lay (2013), which was constrained to have uniform rake. The RMSEs of the vertical and horizontal displacement comparisons are 0.28 and 0.57 m in northern Honshu and 1.53 and 4.82 m offshore. The offshore vertical components are fitted somewhat better by the joint inversion model, but other components are actually better reproduced by TP-MOD. The GPS/Acoustic data are sparse and uncertain, but the large near-trench slip located north of 39°N in TP-MOD does not produce any misfit of the GPS data. The enhanced downdip slip offshore of Fukushima in TP-MOD slightly overpredicts onshore displacements in the south, even though there is a corresponding, but weaker feature in the joint inversion model. The lack of resolution in the teleseismic data for the southern slip could be compensated for by iterating to fit the geodetic data as well, likely by spreading weaker slip over a somewhat larger area. This will require some reconciliation with the tsunami observations, which are already fitted well by TP-MOD. The tsunami waveforms computed for the joint inversion model, shown in Figure S10, give good agreement with the Fukushima records but omit the impulsive peaks at the Iwate and TM buoys. If we had started with the joint inversion model of Yue and Lay (2013) in the present study, the iterative process would have taken longer to achieve the necessary level of near-trench slip for matching the tsunami waveform and runup records in the northern rupture region. The discrepancies with the GPS displacements would largely remain, given the modeling driven by tsunami observations, and can only be resolved by iterative modeling of the combined geodetic, teleseismic, and comprehensive tsunami data sets. That undertaking will make most sense if the issues concerning the contribution of early after-slip and wedge faulting to the offshore displacements can be resolved.

6. Discussion and Conclusions

The dense, continuous records of runup and inundation heights along with the high-resolution topography are instrumental in supplementing the global seismic and near-field water-level records in defining a self-consistent source model through forward tsunami modeling. Our starting rupture model, adapted from a teleseismic inversion, reproduces the near and far-field tsunami amplitude reasonably well, but cannot fully explain the presence or absence of impulsive peaks in the recorded waveforms and the observed runup along the most severely impacted Tohoku coast. The high-resolution model results demonstrate the acute sensitivity of coastal runup to short-period waves generated by near-trench slip, which is responsible for the most devastating impact of the tsunami. The resolved northern near-trench slip is necessary to account for the persistent runup of over 30 m along the Sanriku coast as well as the impulsive leading wave crest recorded at the three GPS buoys immediately offshore. The recorded runup along the south Miyagi and Fukushima coasts provides an important constraint on the southern extent and distribution of the near-trench slip in the main rupture region. The lack of time histories for runup records limits their use in detecting the most tsunamigenic features of the rupture. The shifting and spreading of the epicentral slip patch to the southwest can only be inferred from the initial arrivals at the Fukushima and Central Miyagi GPS buoys. The computed tsunami waveforms and spectra as well as coastal runup heights show strong correlation with the seafloor displacement pattern validating the precise fault slip placement in the final model.

The extension of the iterative approach of Yamazaki, Lay, et al. (2011) to include a stage of direct slip adjustment and high-resolution forward runup modeling is necessary for the Tohoku earthquake and tsunami. The coastal runup data alone do not provide a unique solution, but the iterative process was stabilized by starting with a model that fits the tsunami and seismic waveforms as well as by checking the final model with the GPS and seismic data, both of which narrow the parameter space and reduce the overall uncertainty. As tsunami waves have much slower propagation speeds than earthquake rupture and the computed waveforms are sensitive to model assumptions, the seismic data can provide constraints on the time window for tsunami excitation to avoid an ill-posed problem in the source reconstruction. The procedure adopted here allows high weight to be placed on details of the tsunami runup observations that are difficult to include in any

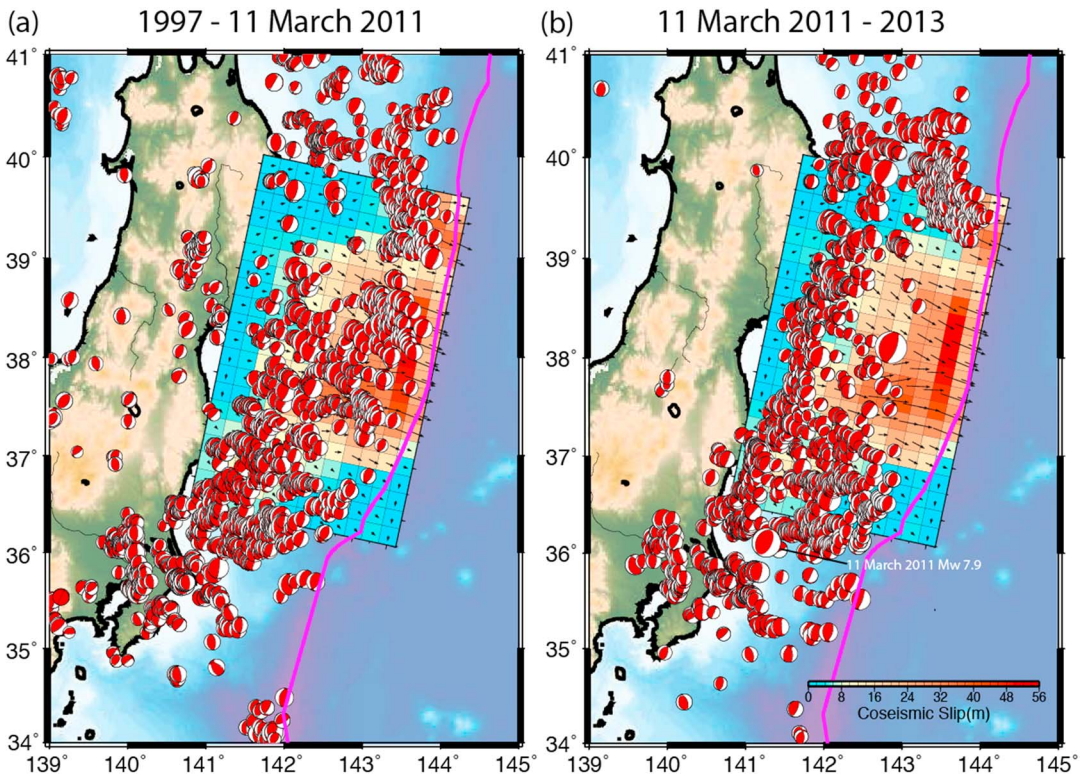

Figure 11. Comparison of the final model TP-MOD with the distribution of thrust-faulting moment tensors from the NIED database. (a) Fourteen years preceding the 11 March 2011 mainshock. (b) Aftershock seismicity through 2013. Mechanism radius is scaled proportional to magnitude. Note the remarkable deficiency of aftershock activity in the large-slip region of the model extending to near the trench (magenta line).

linearized inversion or to emphasize in joint inversions with other data. The fits obtained to the tsunami waveforms are as good as those from direct tsunami inversion by Satake et al. (2013) using Green's functions from a hydrostatic shallow-water model. The use of a nonhydrostatic model with kinematic seafloor deformation in this study provides a more precise account of the near-field waveforms, which in turn can better infer the fault-slip distribution and timing (Li et al., 2016). In our prior applications of the iterative inversion and forward modeling approach for smaller events, excellent fits to the tsunami waveforms were achieved without directly adjusting the slip distribution. The 2011 Tohoku event is so large and complex, and has such limited constraints from seismic data due to the great width of the fault plane and the concentration of slip far from the coast, that the high-resolution forward modeling stage is very beneficial. The adjustments through tsunami modeling help stabilize portions of the null space of the seismic inversion. The final model provides reasonable predictions of geodetic deformations, but comparable iterative modeling incorporating all three data sets would be required for a truly unified model.

The final fault model from our iterative procedure is shown along with NIED (National Research Institute for Earth Science and Disaster Resilience) moment tensor inversions in Figures 11a and 11b for earthquakes having thrust-faulting focal mechanisms in the 14 years prior to the main shock and for the aftershock sequence through 2013. We restrict the focal mechanisms to shallow thrust faulting solutions to exclude events that are clearly not on the megathrust. Some of the thrust events shown are intraplate, but those near the main shock are likely on the plate boundary. The aftershocks in Figure 11b show remarkable deficiency of activity in the large-slip region near the trench, consistent with early findings of Asano et al. (2011), Hasegawa et al. (2012), and many others. This is commonly observed for large thrust events in subduction zones and presents an approach for confirming large-slip regions. The midfault region with increased slip near 37.5°N, relative to the starting model (Figure 9a), has modest levels of aftershock activity. The M_w 7.9 aftershock of 11 March 2011 locates just southwest of the fault model, and aftershock activity in this region is likely associated with its rupture. Note the large concentration of aftershock activity near 39.5°N extending toward the trench. This region, which had an M_w ~ 8.0 event on 20 March 1960 and M_w 6.9 ruptures in 1989 and 1992 just downdip of

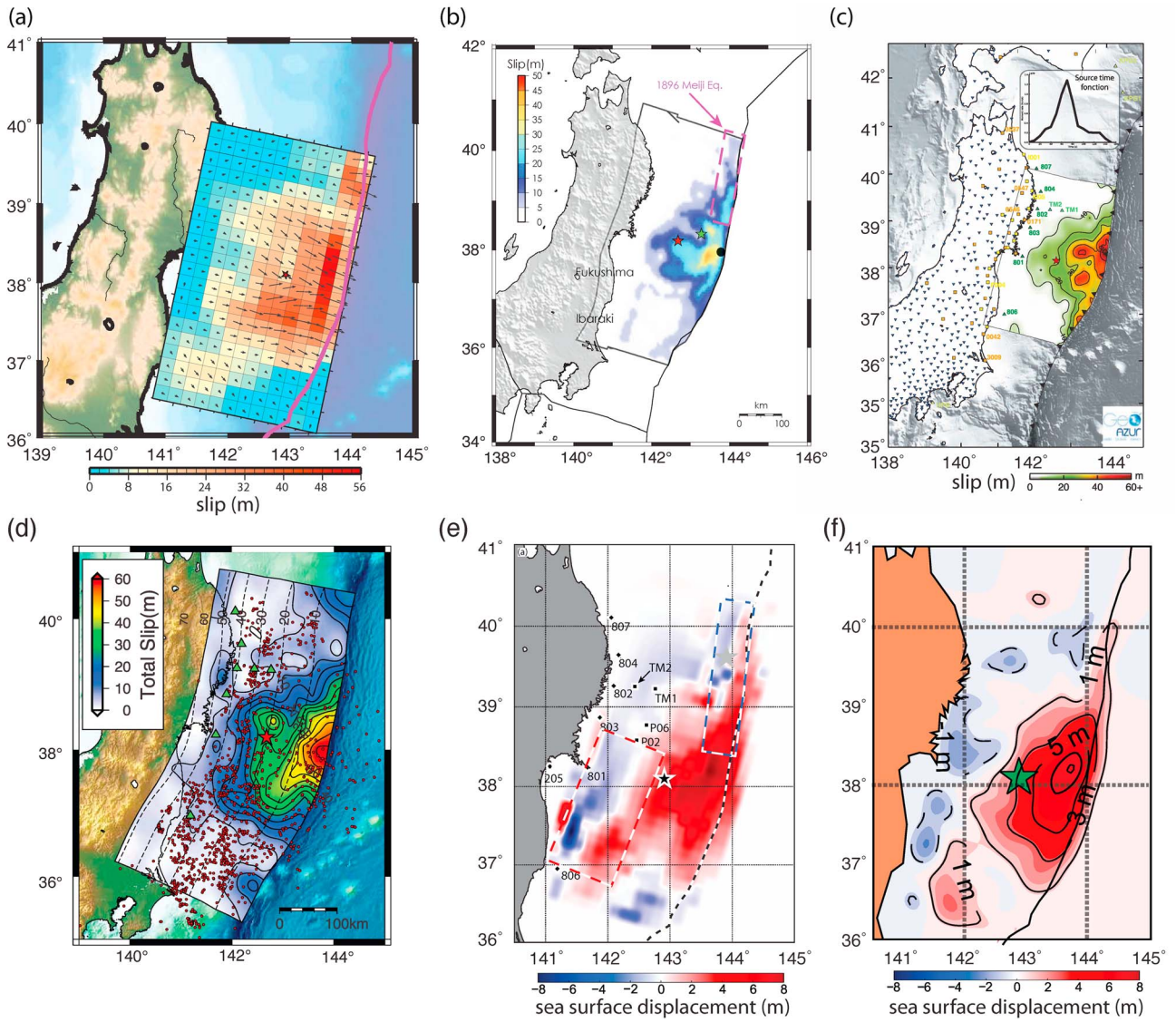

Figure 12. Comparison of fault-slip and initial sea-surface distributions. (a) Final model TP-MOD. (b) Joint inversion of tsunami waveform and geodetic data by Romano et al. (2014). (c) Joint inversion of seismic, horr-GPS, static GPS, seafloor geodesy and tsunami waveform data by Bletery et al. (2014). (d) Joint inversion of seismogeodetic and tsunami waveform data by Melgar and Bock (2015). (e) Posterior median model of initial sea surface displacement from Dettmer et al. (2016) with source areas of the 869 Jogan (red dashed line) and 1896 Sanriku earthquakes (blue dashed line). (f) Cumulative sea surface displacement inverted with variable rupture velocity, dispersive waves and 15 km Gaussian basis functions from Hossen et al. (2015).

the 1896 rupture zone, has enhanced near-trench slip in the final model. The northwest part of the model with relatively few prior events (Figure 11a), identified as the Sanriku Low Seismicity Region by Ye et al. (2011), lies well downdip of the 1896 rupture zone and has diffuse aftershock activity, much of which involves repeating earthquakes (e.g., Uchida et al., 2015). Geodetic measurements indicate several meters of after-slip in this region at depths below 25 km (e.g., Ozawa et al., 2011, 2012). Iinuma et al. (2016) find clear separation between the coseismic and postseismic slip in this region.

The final model TP-MOD indicates large shallow, near-trench slip relative to the initial seismic model in the region from 38.5°N to 39.7°N, where much of the 1896 rupture is thought to have occurred (e.g., Tanioka & Satake, 1996b). Peak slip of ~25–30 m near the trench is inferred, accounting for local sea surface elevation reaching 5.9 m and the huge runup of over 30 m along the Sanriku coast. Figure 12 compares the TP-MOD slip distribution in Figure 12a with several recent models obtained by joint inversions with tsunami waveforms and two reconstructions of initial sea surface perturbation based entirely on tsunami data. The joint inversion models in Figures 12b, 12c, and 12d all have some northward extension of slip beyond 39°N with

Acknowledgments
This study utilized GMT for digital elevation model development and MATLAB for data analysis and presentation. The IRIS DMS data center was used to access the seismic data, while the ARIA GPS coseismic displacement data (version 0.3) were downloaded from ftp://sideshow.jpl.nasa.gov/pub/usrs/ARIA. The GEBCO data were downloaded from http://www.gebco.net/data_and_products/gridded_bathymetry_data/, the 500 m J-EGG500 bathymetry from http://www.jodc.go.jp/data_set/jodc/jegg_intro.html, the digital nautical chart (Electric Reference Charts, new_pec) from http://www.jha.or.jp/en/shop/products/newpec, and the 5 m LiDAR topography from https://fgd.gsi.go.jp/download/mapGis.php?tab=dem. The M7005 digital bathymetry chart was purchased online from http://www.jha.or.jp/shop/index.php?main_page=categories&language=en and the 50 m digital elevation data were purchased from Geospatial Information Authority of Japan (GSI). The recorded DART buoy data were obtained from the National Data Buoy Center at http://www.ndbc.noaa.gov/. The coastal GPS buoys and wave gauges are maintained by Ports and Harbors Bureau, Ministry of Land, Infrastructure, Transport, and Tourism, Japan, and the recorded data were provided by Port and Airport Research Institute, Japan, through http://nowphas.mlit.go.jp/nowphas-data/sub301.htm. The KPG data were obtained from the Japan Agency for Marine-Earth Science and Technology (JAMSTEC) and the Boso and Tokai data from the Japan Meteorological Agency (JMA). A plot of the TM data from http://www.eri.u-tokyo.ac.jp/ was used to digitize the waveforms. The runup and inundation records were downloaded from the 2011 off the Pacific coast of Tohoku Earthquake Tsunami Information website: http://www.coastal.jp/tsunami2011. Y. Yamazaki and K. F. Cheung received support from National Science Foundation RAPID grant CMMI1138710 and National Tsunami Hazard Mitigation Program grant NA15NWS4670025 and T. Lay from National Science Foundation grant EAR1245717. We would like to thank the National Institute for Land and Infrastructure Management and the Building Research Institute, Japan, for the technical support during the June 2011 survey of tsunami damage along the Tohoku coast; Jeremy Bricker and Fumihiko Imamura for the helpful discussions during the field visits to Taro, Aneyoshi, Onagawa, and Kesennuma, in March 2013; and the thoughtful comments from the Associate Editor and the two anonymous reviewers that strengthened the conclusions of this paper. SOEST contribution No. 10287.

5 to 20 m relative displacement near the trench. Initial sea surface perturbation models in Figures 12e and 12f show 1 to 3 m elevations along the trench as well. Many earlier finite source models have no fault slip north of 39°, as mentioned earlier (see a review discussing many models by Lay, 2017), but TP-MOD is in general consistent with the most comprehensive studies of the rupture process that incorporate tsunami observations. Given that the coseismic observations for the GPS/Acoustic data do not extend this far north (Figure 10), and the northernmost GPS/Acoustic data can be well fitted with or without large slip to the north, the geodetic data simply cannot resolve this issue. This study's demonstration that large near-trench slip, as needed to account for the tsunami runup along Sanriku, is compatible with the teleseismic signals is an important contribution to the understanding the 2011 rupture.

At face value, our modeling indicates that the 2011 rupture extended significantly northward with large near-trench slip in addition to having large slip near the trench directly updip of the hypocenter. The large slip indicates the potential for another 1896-style tsunami earthquake is now reduced and further emphasizes the compound nature of the 2011 Tohoku earthquake as a combined rupture of Domain B (main megathrust region) and Domain A (shallow tsunami earthquake region), following the notation of Lay et al. (2012). Post-earthquake offshore GPS/Acoustic measurements, including stations to the north of those shown in Figure 10 (Tomito et al., 2017), are compatible with northward extension of slip at shallow depth to about 39.5°N, although perhaps with lower values ($<$15 m) spread over a larger region. While we cannot uniquely show that our model is the only way to satisfactorily reconcile the seismic and tsunami observations, this study does demonstrate that a self-consistent faulting model can do so, in contrast to the contention of various authors, and that there is no requirement for an exotic source undetected by some of the geophysical measurements to be invoked. Further refinement by direct incorporation of geodetic observations in an iterative modeling undertaking is unlikely to modify this conclusion given the lack of constraint from geodetic data on the near-trench faulting. With the recent deployment of an extensive cabled network of seafloor pressure sensors (S-net) across the entire sedimentary wedge offshore of Honshu, there will be future opportunities to strive for self-consistent models of faulting much more efficiently, potentially in near real-time, so that reliable quantification of the tsunami excitation by faulting or any exotic source can be achieved rapidly.

References

Ammon, C. J., Lay, T., Kanamori, H., & Cleveland, M. (2011). A rupture model of the 2011 off the Pacific coast of Tohoku Earthquake. *Earth, Planets, and Space*, *63*(7), 693–696. https://doi.org/10.5047/eps.2011.05.015

Asano, Y., Saito, T., Ito, Y., Shiomi, K., Hirose, H., Matsumoto, T., … Sekiguchi, S. (2011). Spatial distribution and focal mechanisms of aftershocks of the 2011 off the Pacific coast of Tohoku Earthquake. *Earth, Planets and Space*, *63*(7), 669–673. https://doi.org/10.5047/eps.2011.06.016

Baba, T., Allgeyer, S., Hossen, J., Cummins, P. R., Tsushima, H., Imai, K., … Kato, T. (2017). Accurate numerical simulation of the far-field tsunami caused by the 2011 Tohoku earthquake, including the effects of Boussinesq dispersion, seawater density stratification, elastic loading, and gravitational potential change. *Ocean Modelling*, *111*, 46–54. https://doi.org/10.1016/j.ocemod.2017.01.002

Bai, Y., & Cheung, K. F. (2013). Dispersion and nonlinearity of multi-layer non-hydrostatic free-surface flow. *Journal of Fluid Mechanics*, *726*, 226–260. https://doi.org/10.1017/jfm.2013.213

Bai, Y., & Cheung, K. F. (2016). Hydrostatic versus non-hydrostatic modeling of tsunamis with implications for insular shelf and reef environments. *Coastal Engineering*, *117*, 32–43. https://doi.org/10.1016/j.coastaleng.2016.07.008

Bai, Y., Cheung, K. F., Yamazaki, Y., Lay, T., & Ye, L. (2014). Tsunami surges around the Hawaiian Islands from the 1 April 2014 North Chile M_w 8.1 earthquake. *Geophysical Research Letters*, *41*, 8512–8521. https://doi.org/10.1002/2014GL061686

Bai, Y., Lay, T., Cheung, K. F., & Ye, L. (2017). Two regions of seafloor deformation generated the tsunami for the 13 November 2016, Kaikoura, New Zealand earthquake. *Geophysical Research Letters*, *44*, 6597–6606. https://doi.org/10.1002/2017GL073717

Bai, Y., Yamazaki, Y., & Cheung, K. F. (2015). Interconnection of multi-scale standing waves across the Pacific Basin from the 2011 Tohoku Tsunami. *Ocean Modelling*, *92*, 183–197. https://doi.org/10.1016/j.ocemod.2015.06.007

Bletery, Q., Sladen, A., Delouis, B., Vallée, M., Nocquet, J.-M., Rolland, L., & Jiang, J. (2014). A detailed source model for the M_W 9.0 Tohoku-Oki earthquake reconciling geodesy, seismology and tsunami records. *Journal of Geophysical Research: Solid Earth*, *119*, 7636–7653. https://doi.org/10.1002/2014JB011261

Brown, L., Want, K., & Sun, T. (2015). Static stress drop in the M_W 9 Tohoku-oki earthquake: Heterogeneous distribution and low average value. *Geophysical Research Letters*, *42*, 10,595–10,600. https://doi.org/10.1002/2015GL066361

Cheung, K. F., Bai, Y., & Yamazaki, Y. (2013). Surges around Hawaiian Islands from the 2011 Tohoku tsunami. *Journal of Geophysical Research: Oceans*, *118*, 5703–5719. https://doi.org/10.1002/jgrc.20413

Dettmer, J., Hawkins, R., Cummins, P. R., Hossen, J., Sambridge, M., Hino, R., & Inazu, D. (2016). Tsunami source uncertainty estimation: The 2011 Japan tsunami. *Journal of Geophysical Research: Solid Earth*, *121*, 4483–4505. https://doi.org/10.1002/2015JB012764

Fujii, Y., Satake, K., Sakai, S., Shinohara, M., & Kanazawa, T. (2011). Tsunami source of the 2011 off the Pacific coast of Tohoku, Japan earthquake. *Earth, Planets and Space*, *63*(7), 815–820. https://doi.org/10.5047/eps.2011.06.010

Fujiwara, T., Kodaira, S., No, T., Kaiho, Y., Takahashi, N., & Kaneda, Y. (2011). The 2011 Tohoku-Oki earthquake: Displacement reaching the trench axis. *Science*, *334*(6060), 1240. https://doi.org/10.1126/science.1211554

Grilli, S., Harris, J., Tajallibakhsh, T., Masterlark, T., Kyriakopoulos, C., Kirby, J., & Shi, F. (2013). Numerical simulation of the 2011 Tohoku tsunami based on a new transient FEM co-seismic source: Comparison to far- and near-field observations. *Pure and Applied Geophysics*, *170*(6-8), 1333–1359. https://doi.org/10.1007/s00024-012-0528-y

Gusman, A. R., Tanioka, Y., Sakai, S., & Tsushima, H. (2012). Source model of the great 2011 Tohoku earthquake estimated from tsunami waveforms and crustal deformation data. *Earth and Planetary Science Letters*, *341-344*, 234–242. https://doi.org/10.1016/j.epsl.2012.06.006

Hasegawa, A., Yoshida, K., Asano, Y., Okada, T., Iinuma, T., & Ito, Y. (2012). Change in stress field after the 2011 great Tohoku-Oki earthquake. *Earth and Planetary Science Letters*, *355-356*, 231–243. https://doi.org/10.1016/j.epsl.2012.08.042

Hayashi, Y., Tsushima, H., Hirata, K., Kimura, K., & Maeda, K. (2011). Tsunami source area of the 2011 off the Pacific Coast of Tohoku Earthquake determined from tsunami arrival times at offshore observation stations. *Earth, Planets and Space*, *63*(7), 809–813. https://doi.org/10.5047/eps.2011.06.042

Hayes, G. P. (2011). Rapid source characterization of the 2011 M_W 9.0 off the Pacific coast of Tohoku earthquake. *Earth, Planets and Space*, *63*(7), 529–534. https://doi.org/10.5047/eps.2011.05.012

Hayes, G. P., Wald, D. J., & Johnson, R. L. (2012). Slab1.0: A three-dimensional model of global subduction zone geometries. *Journal of Geophysical Research*, *117*, B01302. https://doi.org/10.1029/2011JB008524

Hino, R. (2015). An overview of the M_W 9, 11 March 2011, Tohoku earthquake. *Summary of the Bulletin of the International Seismological Centre*, *48*, 100–132.

Hooper, A., Pietrzak, J., Simons, W., Cui, H., Riva, R., Naeije, M., … Socquet, A. (2013). Importance of horizontal seafloor motion on tsunami height for the 2011 M_W = 9.0 Tohoku-Oki earthquake. *Earth and Planetary Science Letters*, *361*, 469–479. https://doi.org/10.1016/j.epsl.2012.11.013

Hossen, M. J., Cummins, P. R., Dettmer, J., & Baba, T. (2015). Tsunami waveform inversion for sea surface displacement following the 2011 Tohoku earthquake: Importance of dispersion and source kinematics. *Journal of Geophysical Research: Solid Earth*, *120*, 6452–6473. https://doi.org/10.1002/2015JB011942

Ide, S., Baltay, A., & Beroza, G. C. (2011). Shallow dynamic overshoot and energetic deep rupture in the 2011 M_W 9.0 Tohoku-oki earthquake. *Science*, *332*(6036), 1426–1429. https://doi.org/10.1126/science.1207020

Iinuma, T., Hino, R., Kido, M., Inazu, D., Osada, Y., Ito, Y., … Miura, S. (2012). Coseismic slip distribution of the 2011 off the Pacific coast of Tohoku Earthquake (*M*9.0) refined by means of seafloor geodetic data. *Journal of Geophysical Research*, *117*, B07409. https://doi.org/10.1029/2012JB009186

Iinuma, T., Hino, R., Uchida, N., Nakamura, W., Kido, M., Osada, Y., & Miura, S. (2016). Seafloor observations indicated spatial separation of coseismic and postseismic slips in the 2011 Tohoku earthquake. *Nature Communications*, *7*, 13,506. https://doi.org/10.1038/ncomms13506

Iinuma, T., Ohzono, M., Ohta, Y., & Miura, S. (2011). Coseismic slip distribution of the 2011 off the Pacific coast of Tohoku earthquake (M9.0) estimated based on GPS data—Was the asperity in Miyagi-oki ruptured? *Earth, Planets and Space*, *63*(7), 643–648. https://doi.org/10.5047/eps.2011.06.013

Ito, T., Ozawa, K., Watanabe, T., & Sagiya, T. (2011). Slip distribution of the 2011 off the Pacific coast of Tohoku Earthquake inferred from geodetic data. *Earth, Planets and Space*, *63*(7), 627–630. https://doi.org/10.5047/eps.2011.06.023

Jiang, J., & Simons, M. (2016). Probabilistic imaging of tsunamigenic seafloor deformation during the 2011 Tohoku-oki Earthquake. *Journal of Geophysical Research: Solid Earth*, *121*, 9050–9076. https://doi.org/10.1002/2016JB013760

Kanamori, H. (1972). Mechanism of tsunami earthquakes. *Physics of the Earth and Planetary Interiors*, *6*, 246–259.

Kido, M., Osada, Y., Fujimoto, H., Hino, R., & Ito, Y. (2011). Trench-normal variation in observed seafloor displacements associated with the 2011 Tohoku-Oki earthquake. *Geophysical Research Letters*, *38*, L24303. https://doi.org/10.1029/2011GL050057

Koketsu, K., Yokota, Y., Nishimura, N., Yagi, Y., Miyazaki, S., Satake, K., … Okada, T. (2011). A unified source model for the 2011 Tohoku earthquake. *Earth and Planetary Science Letters*, *310*(3-4), 480–487. https://doi.org/10.1016/j.epsl.2011.09.009

Koper, K. D., Hutko, A. R., Lay, T., Ammon, C. J., & Kanamori, H. (2011). Frequency dependent rupture process of the 2011 M_w 9.0 Tohoku Earthquake: Comparison of short-period *P* wave back-projection images and broadband seismic rupture models. *Earth, Planets, and Space*, *63*(7), 599–602. https://doi.org/10.5047/eps.2011.05.026

Kotani, M., Imamura, F., & Shuto, N. (1998). Tsunami runup simulation and damage estimation by using GIS (in Japanese). *Proceedings of the Coastal Engineering, Japan Society of Civil Engineers*, *45*, 356–360.

Kubo, H., & Kakehi, Y. (2013). Source process of the 2011 Tohoku earthquake estimated from the joint inversion of teleseismic body waves and geodetic data including seafloor observation data: Source model with enhanced reliability by using objectively determined inversion settings. *Bulletin of the Seismological Society of America*, *103*(2B), 1195–1220. https://doi.org/10.1785/0120120113

Lay, T. (2017). A review of the rupture characteristics of the 2011 Tohoku-oki Mw 9.1 earthquake. *Tectonophysics*. https://doi.org/10.1016/j.tecto.2017.09.022

Lay, T., Ammon, C. J., Kanamori, H., Xue, L., & Kim, M. J. (2011). Possible large near-trench slip during the 2011 M_w 9.0 off the Pacific coast of Tohoku earthquake. *Earth, Planets and Space*, *63*(7), 687–692. https://doi.org/10.5047/eps.2011.05.033

Lay, T., Kanamori, H., Ammon, C. J., Koper, K. D., Hutko, A. R., Ye, L., … Rushing, T. M. (2012). Depth-varying rupture properties of subduction zone megathrust faults. *Journal of Geophysical Research*, *117*, B04311. https://doi.org/10.1029/2011JB009133

Lay, T., Yamazaki, Y., Ammon, C. J., Cheung, K. F., & Kanamori, H. (2011). The 2011 M_w 9.0 off the Pacific coast of Tohoku Earthquake: Comparison of deep-water tsunami signals with finite-fault rupture model predictions. *Earth, Planets and Space*, *63*(7), 797–801. https://doi.org/10.5047/eps.2011.05.030

Lay, T., Ye, L., Kanamori, H., Yamazaki, Y., Cheung, K. F., & Ammon, C. J. (2013). The February 6, 2013 M_W 8.0 Santa Cruz Islands earthquake and tsunami. *Tectonophysics*, *608*, 1109–1121. https://doi.org/10.1016/j.tecto.2013.07.001

Lay, T., Ye, L., Kanamori, H., Yamazaki, Y., Cheung, K. F., Kwong, K., & Koper, K. D. (2013). The October 28, 2012 M_W 7.8 Haida Gwaii underthrusting earthquake and tsunami: Slip partitioning along the Queen Charlotte Fault transpressional plate boundary. *Earth and Planetary Science Letters*, *375*, 57–70. https://doi.org/10.1016/j.epsl.2013.05.005

Lee, S.-J. (2011). Rupture process of the 2011 Tohoku-oki earthquake based upon joint source inversion of teleseismic and GPS data. *Terrestrial, Atmospheric and Oceanic Sciences*, *23*(1), 1–7.

Lee, S.-J., Huang, B.-S., Ando, M., Chiu, H.-C., & Wang, J.-H. (2011). Evidence of large scale repeating slip during the 2011 Tohoku-oki earthquake. *Geophysical Research Letters*, *38*, L19306. https://doi.org/10.1029/2011GL049580

Li, L., Cheung, K. F., Yue, H., Lay, T., & Bai, Y. (2016). Effects of dispersion in tsunami Green's functions and implications for joint inversion with seismic and geodetic data: A case study of the 2010 Mentawai M_w 7.8 earthquake. *Geophysical Research Letters*, *43*, 11,182–11,191. https://doi.org/10.1002/2016GL070970

Lorito, S., Romano, F., & Lay, T. (2016). Tsunamigenic major and great earthquakes (2004–2013): Source processes inverted from seismic, geodetic, and sea-level data. In *Encyclopedia of complexity and systems science* (pp. 1–52). New York: Springer. https://doi.org/10.1007/978-3-642-27737-5_641-1

Løvholt, F., Kaiser, G., Glimsdal, S., Scheele, L., Harbitz, C. B., & Pedersen, G. (2012). Modeling propagation and inundation of the 11 March 2011 Tohoku tsunami. *Natural Hazards and Earth System Science*, *12*(4), 1017–1028. https://doi.org/10.5194/nhess-12-1017-2012

MacInnes, B. T., Gusman, A. R., LeVeque, R. J., & Tanioka, Y. (2013). Comparison of earthquake source models for the 2011 Tohoku event using tsunami simulations and near-field observations. *Bulletin of the Seismological Society of America*, *103*, 1256–1274. https://doi.org/10.1785/0120120121

Maeda, T., Furumura, T., Sakai, S., & Shinohara, M. (2011). Significant tsunami observed at ocean-bottom pressure gauges during the 2011 off the Pacific coast of Tohoku earthquake. *Earth, Planets and Space*, *63*(7), 803–808. https://doi.org/10.5047/eps.2011.06.005

Masterlark, T. (2003). Finite element model predictions of static deformation from dislocation sources in a subduction zone: Sensitivities to homogeneous, isotropic, Poisson-solid, and half-space assumptions. *Journal of Geophysical Research*, *108*(B11), 2540. https://doi.org/10.1029/2002JB002296

Melgar, D., & Bock, Y. (2015). Kinematic earthquake source inversion and tsunami runup prediction with regional geophysical data. *Journal of Geophysical Research: Solid Earth*, *120*, 3324–3349. https://doi.org/10.1002/2014JB011832

Minson, S. E., Simons, M., Beck, J. L., Ortega, F., Jiang, J., Owen, S. E., … Sladen, A. (2014). Bayesian inversion for finite fault earthquake source models—II: The 2011 great Tohoku-Oki, Japan earthquake. *Geophysical Journal International*, *198*(2), 922–940. https://doi.org/10.1093/gji/ggu170

Miyazaki, S., McGuire, J. J., & Segall, P. (2011). Seismic and aseismic fault slip before and during the 2011 off the Pacific coast of Tohoku earthquake. *Earth, Planets and Space*, *63*(7), 637–642. https://doi.org/10.5047/eps.2011.07.001

Mori, N., Takahashi, T., & the 2011 Tohoku Earthquake Tsunami Joint Survey Group (2012). Nationwide post event survey and analysis of the 2011 Tohoku earthquake tsunami. *Coastal Engineering Journal*, *54*(01), 1250001. https://doi.org/10.1142/S0578563412500015

Mori, N., Takahashi, T., Yasuda, T., & Yanagisawa, H. (2011). Survey of 2011 Tohoku earthquake tsunami inundation and run-up. *Geophysical Research Letters*, *38*, L00G14. https://doi.org/10.1029/2011GL049210

Murashima, Y., Takeuchi, H., Imamura, F., Koshimura, S., Fujiwara, K., & Suzuki, T. (2008). Study on topographic model using LiDAR for tsunami simulation. In *Proceedings of ISPRS XXXVII(B8)* (pp. 223–228). Beijing.

Noda, H., Lapusta, N., & Kanamori, H. (2013). Comparison of average stress drop measures for ruptures with heterogeneous stress change and implications for earthquake physics. *Geophysical Journal International*, *193*(3), 1691–1712. https://doi.org/10.1093/gji/ggt074

Okada, Y. (1992). Internal deformation due to shear and tensile faults in a half-space. *Bulletin of the Seismological Society of America*, *82*(2), 1018–1040.

Ozawa, S., Nishimura, T., Munekane, H., Suito, H., Kobayashi, T., Tobita, M., & Imakiire, T. (2012). Preceding, coseismic, and postseismic slips of the 2011 Tohoku earthquake, Japan. *Journal of Geophysical Research*, *117*, B07404. https://doi.org/10.1029/2011JB009120

Ozawa, S., Nishimura, T., Suito, H., Kobayahi, T., Tobita, M., & Imakiire, T. (2011). Coseismic and postseismic slip of the 2011 magnitude-9 Tohoku-oki earthquake. *Nature*, *475*(7356), 373–376. https://doi.org/10.1038/nature10227

Pollitz, F., Bürgmann, R., & Banerjee, P. (2011). Geodetic slip model of the 2011 M9.0 Tohoku earthquake. *Geophysical Research Letters*, *38*, L00G08. https://doi.org/10.1029/2011GL048632

Ren, Z., Wang, B., Fan, T., & Liu, H. (2013). Numerical analysis of impacts of 2011 Japan Tohoku tsunami on China Coast. *Journal of Hydrodynamics, Series B*, *25*(4), 580–590. https://doi.org/10.1016/S1001-6058(11)60399-6

Romano, F., Piatanesi, A., Lorito, S., D'Agostino, N., Hirata, K., Atzori, S., … Cocco, M. (2012). Clues from joint inversion of tsunami and geodetic data of the 2011 Tohoku-oki earthquake. *Scientific Reports*, *2*(1), 385. https://doi.org/10.1038/srep00385

Romano, F., Trasatti, E., Lorito, S., Piromallo, C., Piatanesi, A., Ito, Y., … Cocco, M. (2014). Structural control on the Tohoku earthquake rupture process investigated by 3D FEM, tsunami and geodetic data. *Scientific Reports*, *4*(1), 5631. https://doi.org/10.1038/srep05631

Saito, T., Ito, Y., Inazu, D., & Hino, R. (2011). Tsunami source of the 2011 Tohoku-Oki earthquake, Japan: Inversion analysis based on dispersive tsunami simulations. *Geophysical Research Letters*, *38*, L00G19. https://doi.org/10.1029/2011GL049089

Satake, K., Fujii, Y., Harada, T., & Namegaya, Y. (2013). Time and space distribution of coseismic slip of the 2011 Tohoku earthquake as inferred from tsunami waveform data. *Bulletin of the Seismological Society of America*, *103*(2B), 1473–1492. https://doi.org/10.1785/0120120122

Sato, M., Ishikawa, T., Ujihara, N., Yoshida, S., Fujita, M., Mochizuki, M., & Asada, A. (2011). Displacement above the hypocenter of the 2011 Tohoku-Oki earthquake. *Science*, *332*(6036), 1395–1395. https://doi.org/10.1126/science.1207401

Shao, G., Li, X., Ji, C., & Maeda, T. (2011). Focal mechanism and slip history of the 2011 M_W 9.1 off the Pacific coast of Tohoku Earthquake, constrained with teleseismic body and surface waves. *Earth, Planets and Space*, *63*(7), 559–564. https://doi.org/10.5047/eps.2011.06.028

Simons, M., Minson, S. E., Sladen, A., Ortega, F., Jiang, J., Owen, S. E., … Webb, F. H. (2011). The 2011 magnitude 9.0 Tohoku-oki earthquake: Mosaicking the megathrust from seconds to centuries. *Science*, *332*(6036), 1421–1425. https://doi.org/10.1126/science.1206731

Sun, T., Wang, K., Fujiwara, T., Kodaira, S., & He, J. (2017). Large fault sip peaking at trench in the 2011 Tohoku-oki earthquake. *Nature Communications*, *8*, 4044. https://doi.org/10.1038/ncomms14044

Suppasri, A., Koshimura, S., Imai, K., Mas, E., Gokon, H., Muhari, A., & Imamura, F. (2012). Damage characteristic and field survey of the 2011 Great East Japan Tsunami in Miyagi Prefecture. *Coastal Engineering Journal*, *54*(01), 1250005. https://doi.org/10.1142/S0578563412500052

Tajima, F., Mori, J., & Kennett, B. L. N. (2013). A review of the 2011 Tohoku-Oki earthquake (M_W 9.0): Large-scale rupture across heterogeneous plate coupling. *Tectonophysics*, *586*, 15–34. https://doi.org/10.1016/j.tecto.2012.09.014

Tang, L., Titov, V. V., Bernard, E. N., Wei, Y., Chamberlin, C. D., Newman, J. C., … Gica, E. (2012). Direct energy estimation of the 2011 Japan tsunami using deep-ocean pressure measurements. *Journal of Geophysical Research*, *117*, C08008. https://doi.org/10.1029/2011JC007635

Tanioka, Y., & Satake, K. (1996a). Tsunami generation by horizontal displacement of ocean bottom. *Geophysical Research Letters*, *23*(8), 861–864. https://doi.org/10.1029/96GL00736

Tanioka, Y., & Satake, K. (1996b). Fault parameters of the 1896 Sanriku tsunami earthquake estimated from tsunami numerical modeling. *Geophysical Research Letters*, *23*(13), 1549–1552. https://doi.org/10.1029/96GL01479

Tappin, D. R., Grilli, S. T., Harris, J. C., Geller, R. J., Masterlark, T., Kirby, J. T., … Mai, P. M. (2014). Did a submarine landslide contribute to the 2011 Tohoku tsunami? *Marine Geology*, *357*, 344–361. https://doi.org/10.1016/j.margeo.2014.09.043

Tomito, F., Kido, M., Ohta, Y., Iinuma, T., & Hino, R. (2017). Along-trench variation in seafloor displacements after the 2011 Tohoku earthquake. *Science Advances*, *3*(7), e1700113. https://doi.org/10.1126/sciadv.1700113

Tsai, V. C., Ampuero, J. P., Kanamori, H., & Stevenson, D. J. (2013). Estimating the effect of earth elasticity and variable water density on tsunami speeds. *Geophysical Research Letters*, *40*, 492–496. https://doi.org/10.1002/grl.50147

Uchida, N., Shimamura, K., Matsuzawa, T., & Okada, T. (2015). Postseismic response of repeating earthquakes around the 2011 Tohoku-oki earthquake: Moment increases due to the fast loading rate. *Journal of Geophysical Research: Solid Earth*, *120*, 259–274. https://doi.org/10.1002/2013JB010933

Wei, S., Graves, R., Helmberger, D., Avouac, J.-P., & Jiang, J. (2012). Sources of shaking and flooding during the Tohoku-Oki earthquake: A mixture of rupture styles. *Earth and Planetary Science Letters*, *333-334*, 91–100. https://doi.org/10.1016/j.epsl.2012.04.006

Wei, Y., Chamberlin, C., Titov, V. V., Tang, L., & Bernard, E. N. (2013). Modeling of the 2011 Japan tsunami: Lessons for near-field forecast. *Pure and Applied Geophysics*, *170*(6-8), 1309–1331. https://doi.org/10.1007/s00024-012-0519-z

Wessel, P., & Smith, W. H. F. (1995). New version of the Generic Mapping Tools released. *Eos, Transactions American Geophysical Union*, *76*(33), 329. https://doi.org/10.1029/95EO00198

Yagi, Y., & Fukahata, Y. (2011). Rupture process of the 2011 Tohoku-Oki earthquake and absolute elastic strain release. *Geophysical Research Letters*, *38*, L19307. https://doi.org/10.1029/2011GL048701

Yamazaki, Y., Cheung, K. F., & Kowalik, Z. (2011). Depth-integrated, non-hydrostatic model with grid nesting for tsunami generation, propagation, and run-up. *International Journal for Numerical Methods in Fluids*, *67*(12), 2081–2107. https://doi.org/10.1002/fld.2485

Yamazaki, Y., Cheung, K. F., Kowalik, Z., Lay, T., & Pawlak, G. (2012). NEOWAVE. In *Proceedings and Results of the NTHMP Model Benchmarking Workshop* (pp. 239–302). Galveston, TX: NOAA Special Report.

Yamazaki, Y., Cheung, K. F., & Lay, T. (2013). Modeling of the 2011 Tohoku near-field tsunami from finite-fault inversion of seismic waves. *Bulletin of the Seismological Society of America*, *103*(2B), 1444–1455. https://doi.org/10.1785/0120120103

Yamazaki, Y., Cheung, K. F., Pawlak, G., & Lay, T. (2012). Surges along the Honolulu coast from the 2011 Tohoku tsunami. *Geophysical Research Letters*, *39*, L09604. https://doi.org/10.1029/2012GL051624

Yamazaki, Y., Kowalik, Z., & Cheung, K. F. (2009). Depth-integrated, non-hydrostatic model for wave breaking and run-up. *International Journal for Numerical Methods in Fluids*, *61*(5), 473–497. https://doi.org/10.1002/fld.1952

Yamazaki, Y., Lay, T., Cheung, K. F., Yue, H., & Kanamori, H. (2011). Modeling near-field tsunami observations to improve finite-fault slip models for the 11 March 2011 Tohoku earthquake. *Geophysical Research Letters*, *38*, L00G15. https://doi.org/10.1029/2011GL049130

Ye, L., Kanamori, H., Avouac, J.-P., Li, L., Cheung, K. F., & Lay, T. (2016). The 16 April 2016, M_W 7.8 (M_S 7.5) Ecuador earthquake: A quasi-repeat of the 1942 M_S 7.5 earthquake and partial re-rupture of the 1906 M_S 8.6 Colombia-Ecuador earthquake. *Earth and Planetary Science Letters*, *454*, 248–258. https://doi.org/10.1016/j.epsl.2016.09.006

Ye, L., Lay, T., & Kanamori, H. (2011). The Sanriku-Oki low-seismicity region on the northern margin of the great 2011 Tohoku-Oki earthquake rupture. *Journal of Geophysical Research*, *117*, B02305. https://doi.org/10.1029/2011JB008847

Ye, L., Lay, T., Kanamori, H., & Rivera, L. (2016). Rupture characteristics of major and great ($M_W \geq 7.0$) megathrust earthquakes from 1990 to 2015: 1. Source parameter scaling relationships. *Journal of Geophysical Research: Solid Earth*, *121*, 826–844. https://doi.org/10.1002/2015JB012426

Yokota, Y., Koketsu, K., Fujii, Y., Satake, K., Sakai, S., Shinohara, M., & Kanazawa, T. (2011). Joint inversion of strong motion, teleseismic, geodetic, and tsunami datasets for the rupture process of the 2011 Tohoku earthquake. *Geophysical Research Letters*, *38*, L00G21. https://doi.org/10.1029/2011GL050098

Yoshida, Y., Ueno, H., Muto, D., & Aoki, S. (2011). Source process of the 2011 off the Pacific coast of Tohoku earthquake with the combination of teleseismic and strong motion data. *Earth, Planets and Space*, *63*(7), 565–569. https://doi.org/10.5047/eps.2011.05.011

Yue, H., & Lay, T. (2011). Inversion of high-rate (1 sps) GPS data for rupture process of the 11 March 2011 Tohoku earthquake (M_w 9.1). *Geophysical Research Letters*, *38*, L00G09. https://doi.org/10.1029/2011GL048700

Yue, H., & Lay, T. (2013). Source rupture models for the M_w 9.0 2011 Tohoku earthquake from joint inversions of high-rate geodetic and seismic data. *Bulletin of the Seismological Society of America*, *103*(2B), 1242–1255. https://doi.org/10.1785/0120120119

Yue, H., Lay, T., Li, L., Yamazaki, Y., Cheung, K. F., Rivera, L., … Muhari, A. (2015). Validation of linearity assumptions for using tsunami waveforms in joint inversion of kinematic rupture models: Application to the 2010 Mentawai M_w 7.8 tsunami earthquake. *Journal of Geophysical Research: Solid Earth*, *120*, 1728–1747. https://doi.org/10.1002/2014JB011721

Yue, H., Lay, T., Rivera, L., Bai, Y., Yamazaki, Y., Cheung, K. F., … Muhari, A. (2014). Rupture process of the 2010 M_w 7.8 Mentawai tsunami earthquake from joint inversions of near-field hr-GPS and teleseismic body wave recordings constrained by tsunami observations. *Journal of Geophysical Research: Solid Earth*, *119*, 5574–5593. https://doi.org/10.1002/2014JB011082